https://doi.org/10.3847/1538-4357/ab245b

CrossMark

The Planetary Accretion Shock. II. Grid of Postshock Entropies and Radiative Shock Efficiencies for Nonequilibrium Radiation Transport

Gabriel-Dominique Marleau[1,2,3] , Christoph Mordasini[1] , and Rolf Kuiper[2,3]

[1] Physikalisches Institut, Universität Bern, Gesellschaftsstr. 6, 3012 Bern, Switzerland; gabriel.marleau@uni-tuebingen.de
[2] Institut für Astronomie und Astrophysik, Eberhard Karls Universität Tübingen, Auf der Morgenstelle 10, D-72076 Tübingen, Germany
[3] Max-Planck-Institut für Astronomie, Königstuhl 17, D-69117 Heidelberg, Germany

Abstract

In the core-accretion formation scenario of gas giants, most of the gas accreting onto a planet is processed through an accretion shock. In this series of papers we study this shock because it is key in setting the structure of the forming planet and thus its postformation luminosity, with dramatic observational consequences. We perform one-dimensional gray radiation-hydrodynamical simulations with nonequilibrium (two-temperature) radiation transport and up-to-date opacities. We survey the parameter space of accretion rate, planet mass, and planet radius and obtain postshock temperatures, pressures, and entropies, as well as global radiation efficiencies. We find that the shock temperature $T_{\rm shock}$ is usually given by the "free-streaming" limit. At low temperatures the dust opacity can make the shock hotter but not significantly so. We corroborate this with an original semianalytical derivation of $T_{\rm shock}$. We also estimate the change in luminosity between the shock and the nebula. Neither $T_{\rm shock}$ nor the luminosity profile depend directly on the optical depth between the shock and the nebula. Rather, $T_{\rm shock}$ depends on the immediate preshock opacity, and the luminosity change on the equation of state. We find quite high immediate postshock entropies ($S \approx 13$–$20\,k_{\rm B}\,m_{\rm H}^{-1}$), which makes it seem unlikely that the shock can cool the planet. The global radiation efficiencies are high ($\eta^{\rm phys} \gtrsim 97\%$), but the remainder of the total incoming energy, which is brought into the planet, exceeds the internal luminosity of classical cold starts by orders of magnitude. Overall, these findings suggest that warm or hot starts are more plausible.

Key words: accretion, accretion disks – methods: analytical – methods: numerical – planets and satellites: formation – planets and satellites: gaseous planets – radiative transfer

1. Introduction

With its first direct detections already some 10 to 15 years ago (Chauvin et al. 2004; Marois et al. 2008), the technique of direct imaging has started to reveal a scarce but interesting population of planets or substellar objects of very low mass at large separations from their host stars (Bowler 2016; Bowler & Nielsen 2018; Wagner et al. 2019). The formation mechanism of individual detections is often not obvious, but gravitational instability as well as core accretion (with the inclusion of N-body interactions during the formation phase and in the first few million years afterward) are likely candidates to explain the origin of at least some of these systems (e.g., Marleau et al. 2019). These different formation pathways may imprint into the observed brightness of the planets (Baruteau et al. 2016; Mordasini et al. 2017).

To interpret the brightness measurements requires knowing the postformation luminosity of planets of different masses. Formation models, principally those of the California (Pollack et al. 1996; Bodenheimer et al. 2000, 2013; Marley et al. 2007; Lissauer et al. 2009) and the Bern group (Alibert et al. 2005; Mordasini et al. 2012a, 2012b, 2017), seek to predict this luminosity within the approximation of spherical accretion. They need to assume something about the efficiency of the gas-accretion shock at the surface of the planet during runaway gas accretion. This efficiency is defined as the fraction of the total energy influx that is reradiated into the local disk and thus does not end up being added to the planet. The extremes are known

as "cold starts" and "hot starts" (Marley et al. 2007), and their postformation luminosities can differ by orders of magnitude.

In a recent series of papers, Berardo et al. (2017), Berardo & Cumming (2017), and Cumming et al. (2018) have begun calculating the structure of accreting planets following Stahler (1988). Crucially, they take into account that in the settling zone below the shock, the continuing compression of the postshock layers leads to a nonconstant luminosity. They find that the thermal influence of the shock on the evolution of the planet during accretion depends on the contrast between the entropy of the (outer convective zone of the) planet and that of the postshock gas. This approach promises eventually to lead to more realistic predictions of the postformation luminosity[4] but does require, as a boundary condition, knowledge of the temperature of the shock.

While global three-dimensional (radiation-)hydrodynamical simulations of the protoplanetary and of the circumplanetary disks (Klahr & Kley 2006; Machida et al. 2008; Tanigawa et al. 2012; D'Angelo & Bodenheimer 2013; Szulágyi et al. 2016, 2017) have the potential of providing a realistic answer as to the postshock conditions and its efficiency, they still have a limited spatial resolution of $\Delta x \sim 1\,R_{\rm J}$ at best at the position of the planet, despite their high dynamical range of spatial scales. Also due to the computational cost, they are (currently) unable to survey the large input parameter space, which covers a factor of a few in planet radius, an order of magnitude in mass, and several orders or magnitude in accretion rate and internal luminosity (e.g., Mordasini et al. 2012b, 2017).

---

[4] This statement holds for a given an accretion history, which, admittedly, is, however uncertain since it depends in part on the migration behavior of the planet, which itself is fraught with uncertainty.

In the present series of papers, we use one-dimensional models of the gas accretion to take a careful look at shock microphysics. In Marleau et al. (2017, hereafter Paper I), we introduced our approach, presented a detailed analysis of results for one combination of formation parameters, and discussed the shock efficiency for a certain range of parameters. However, we restricted ourselves to equilibrium radiation transport, in which the gas and radiation temperatures are assumed to be equal everywhere, and assumed a perfect[5] equation of state (EOS), i.e., a constant mean molecular weight μ and heat capacity ratio[6] γ. We found that the shock is isothermal and supercritical and that the efficiencies can be as low as 40%.

Here, we relax the assumption of equilibrium radiation transport, look more carefully at the role of opacity, and consider a wider parameter space than in Paper I, exploring systematically the dependence on accretion rate, mass, and planet radius. We also extend our analytical derivations considerably. We again assume a perfect EOS, varying μ and γ, and focus on the cases in which the internal luminosity $L_{\rm int}$ is much lower than the shock luminosity $L_{\rm acc}$.

This paper is structured as follows: in Section 2 we estimate in what regions of ($\dot{M}$, $M_{\rm p}$, $R_{\rm p}$, $L_{\rm int}$), where $\dot{M}$ is the accretion rate while $M_{\rm p}$ and $R_{\rm p}$ are the planet mass and radius, the assumption $L_{\rm int} \ll L_{\rm acc}$ holds, which guides our choice of parameters. Section 3 briefly reviews our setup and details the relevant microphysics, including the updated opacities. The main thrust of this paper is in Section 4, which presents and analyzes results, including shock temperatures, global radiative shock efficiencies, and postshock entropies, for a grid of simulations. In Section 5 we present semianalytical derivations of the shock temperature and of the temperature profile in the accretion flow and compare them to our results. In Section 6 we carefully investigate the effect of different perfect EOS in nonequilibrium radiation transport and of dust destruction in the Zel'dovich spike. This motivates us to derive analytically the drop or increase of the luminosity across the Hill sphere. While we do not yet calculate the structure of forming planets using our shock results, Section 7 explores whether hot or cold starts are expected, and presents a further discussion. Finally, Section 8 summarizes this work and presents our conclusions.

2. Estimate of Negligible Internal Luminosity

The main formation parameters are the accretion rate onto the planet, the planet mass, the planet radius, and the internal luminosity of the planet, denoted by $\dot{M}$, $M_{\rm p}$, $R_{\rm p} = r_{\rm shock}$ (the position of the shock $r_{\rm shock}$ defining the radius of the very nearly hydrostatic protoplanet), and $L_{\rm int}$, respectively. In Paper I and this work, we focus on the case of negligible $L_{\rm int}$. This luminosity comes from the contraction and cooling of the planet interior and is generated almost entirely within a small fraction of the planetary volume, where most of the mass resides. Specifically, this means $L_{\rm int} \ll \Delta L$, where the luminosity jump at the shock $\Delta L \sim L_{\rm acc}$. This reduces the number of free parameters in our study, but is mainly also expected to be the limit in which the shock simulations we perform are the most relevant.
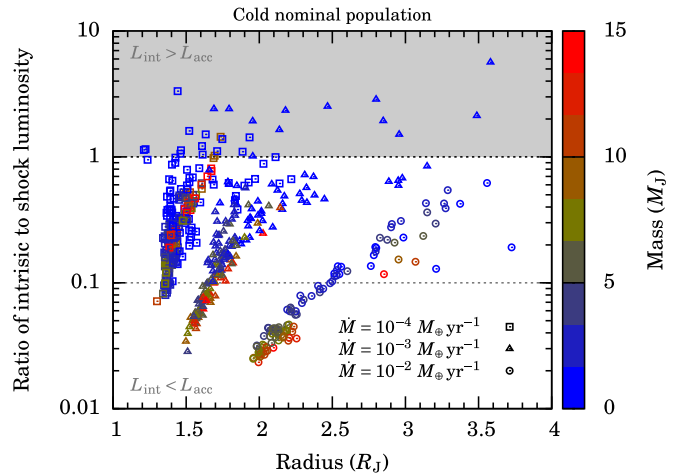

Figure 1. Ratio of intrinsic to shock luminosity in the cold nominal population syntheses of Mordasini et al. (2017). The color of the points encodes the mass; planets between $M_{\rm p} = 0.3$ and $15\ M_{\rm J}$ are shown. The three groups of points are for accretion rates of $\dot{M} = 10^{-4}$–$10^{-2}\ M_\oplus\ {\rm yr}^{-1}$ within 0.05 dex (left to right; see legend).

We can estimate in what cases neglecting the interior luminosity should be best justified. In the Marley et al. (2007) formation calculations, which represent the extreme case of cold accretion (Mordasini et al. 2017), it is blatantly obvious that $L_{\rm int}$ is negligible compared to $L_{\rm acc}$ (see their Figure 3 and the discussion in Section 7.1). For more "moderate" (i.e., warmer) versions of cold starts, Figure 1 shows the ratio $L_{\rm int}/L_{\rm acc}$ for cold-start population synthesis planets as in Figure 7(d) of (Mordasini et al. 2017). Most points are below $L_{\rm int}/L_{\rm acc} \sim 1$. Overall, the higher the accretion rate or the mass, the less important the interior luminosity. Using the hot-start population should yield a somewhat weaker shock because the radii are larger (leading to the "core mass effect"; Mordasini 2013), but overall the results should be similar (see Figure 13 of Mordasini et al. 2017).

When we focus on $\dot{M} \gtrsim 10^{-3}\ M_\oplus\ {\rm yr}^{-1}$ and masses above a few $M_{\rm J}$, simulations with $R_{\rm p} \approx 1.5$–$3\ R_{\rm J}$ should be those in which the accretion shock is the most relevant. At $\dot{M} \lesssim 10^{-4}\ M_\oplus\ {\rm yr}^{-1}$, the interior luminosity frequently represents an appreciable fraction of the accretion luminosity, even up to high planet masses. Therefore we do not consider these lower rates in this paper. Of course, this estimate is not self-consistent because these formation and evolution calculations assume a fixed shock efficiency $\eta = 100\%$, whereas we find clearly lower values (in the sense that the heating of the planet by the postshock material is important relative to the interior luminosity of the planet; see Section 7.1 and Paper I). Nevertheless, the estimate should provide reasonable guidance.

3. Simulation Approach

As in Paper I, we use the PLUTO code (Mignone et al. 2007, 2012) to solve in a time-explicit fashion for the hydrodynamics. The one-dimensional spherically symmetric mass and momentum conservation equations are

$$\frac{\partial \rho}{\partial t} + \frac{1}{r^2}\frac{\partial}{\partial r}(r^2 \rho v) = 0 \qquad (1a)$$

$$\frac{\partial(\rho v)}{\partial t} + \frac{1}{r^2}\frac{\partial}{\partial r}(r^2 \rho v^2) + \frac{\partial P}{\partial r} = -\rho g, \qquad (1b)$$

---

[5] This is also sometimes termed a "constant EOS" but should not be referred to only as an "ideal gas," as is often done, unfortunately. Indeed, the latter only needs fulfill $P = \rho/(\mu m_{\rm H}) k_{\rm B} T$ with μ not necessarily constant. A nonideal EOS also includes quantum degeneracy effects, for example.

[6] For a perfect EOS, the various adiabatic indices $\Gamma_{1,2,3}$, the heat capacity ratio γ, as well as $\gamma_{\rm eff} \equiv P/e_{\rm int} + 1$, where $e_{\rm int}$ is the internal energy, are all equal. Therefore we always write γ in this paper.

respectively, where P is the pressure and the local gravitational acceleration is $g = |-GM_p/r^2|$, the self-gravity of the gas being negligible. Note that, using mass conservation, the momentum equation can also be written in the form

$$\rho\frac{\partial v}{\partial t} + \rho v\frac{\partial v}{\partial r} + \frac{\partial P}{\partial r} = -\rho g, \qquad (2)$$

i.e., without the geometry factors $r^{\pm 2}$ in the flux term.

The energy equation is similar to what we used in Paper I, but we make use of the newest version of the flux-limited diffusion (FLD) solver `Makemake`. We return to this in Section 3.2.

3.1. Setup

The simulation domain extends from close to the planetary surface to almost out to the "accretion radius" R_{acc} (Bodenheimer et al. 2000; Paper I), near one-third of the Hill radius ($k_{Lissauer} = 1/3$ Lissauer et al. 2009). A grid with 1000 uniformly spaced cells between the inner edge of the domain, r_{min}, and $r_{min} + 0.5\,R_J$ and 1000 geometrically stretched cells from $r_{min} + 0.5\,R_J$ to the outer edge of the domain, r_{max}, was found to yield good results for several parameter combinations. For the other cases, an increase to 2000+2000 cells sufficed to obtain smooth profiles (e.g., in the local accretion rate $\dot{M}(r) = 4\pi r^2 \rho(v)v(r)$ below the shock). We verified that increasing the resolution does not produce different results except for sharpening the Zel'dovich spike (see below) and changing its peak value. Thus there are no qualitative consequences on the pre- or postshock structure.

To avoid numerical issues at early times, we have revised the initial setup. We do not use a hydrostatic atmosphere as was done in Paper I, but rather begin directly with an accretion profile in the density ρ and velocity v. The initial radiation and gas temperatures are set to the nebula temperature $T_{neb} = 150$ K (Pollack et al. 1994) at the outer edge r_{max} and increase linearly up to $1.1T_{neb}$ at r_{min}. The radiation and gas temperatures are set equal, and the initial pressure is obtained from ρ and T_{gas}.

We use a CFL number of 0.8 (we verified that CFL = 0.4 gives identical profiles), and use the `tvdlf` Riemann solver along with the `MinMod` slope limiter. This somewhat diffusive combination ensures numerical stability while not significantly influencing the outcome.

The inner wall is reflective and the radiation flux there is set to zero. We let gas fall in freefall from the outer edge under the action of the central potential, enforcing an accretion rate at the outer edge only. The gas piles up at the bottom of the domain, forming a shock that defines the surface of the planet at $r_{shock} = R_p$ (both variables are used interchangeably throughout, with r_{shock}^- (r_{shock}^+) denoting the downstream (upstream) location). This shock surface often but not always moves outward over time, although at a rate that is slow even compared to the strongly subsonic postshock velocity. The deepest pressure in the atmosphere we simulate is greater than the postshock (ram) pressure by one to several orders of magnitude, depending on the amount of accumulated mass and the local gravitational acceleration $g = GM_p/r^2$, where r is the radial coordinate in spherical geometry, and G is the gravitational constant.

While we use a fully time-dependent code, our simulations represent steady-state snapshots in the formation-parameter space, as discussed in Paper I. For reference, the profiles for the runs presented here needed on the order of 5×10^6 s to come into equilibrium. This is entirely negligible compared to

the timescale on which the protoplanet grows, which is on the order of 10^4–10^6 yr. (Even after $t_{stop} = 2 \times 10^7$ s, our usual stopping time, some starting structures were still visible at a position r deep below the shock for which $t_{stop} \lesssim -\int_r^{r_{shock}} (1/v)\,dx$ in at least some simulations; these regions are not of interest here, however.)

3.2. Radiation Transport

A significant improvement since Paper I is the change from equilibrium to nonequilibrium (or two-temperature, 2-T) FLD in the radiation transport routine `Makemake` (Kuiper et al. 2010, R. Kuiper et al. in preparation) In this approach, the gas and radiation temperatures are not enforced to be equal, and the full energy equation reads (see also Mihalas & Mihalas 1984; Kley 1989; Turner & Stone 2001; R. Kuiper et al. 2010; Commerçon et al. 2011b; Klassen et al. 2014)

$$\frac{\partial(E_{kin} + E_{int})}{\partial t} + \nabla([E_{kin} + E_{int} + P]v) = -\Lambda - \rho g v, \qquad (3a)$$

$$\frac{\partial E_{rad}}{\partial t} + \nabla F_{rad} = +\Lambda, \qquad (3b)$$

omitting the radiation pressure because it is negligible in this problem, and with F_{rad} the radiative flux. In FLD, one writes (Paper I)

$$F_{rad} = -D_F \boldsymbol{\nabla} E_{rad}, \qquad (4a)$$

$$D_F \equiv \frac{\lambda(R)c}{\kappa_R \rho}, \qquad (4b)$$

$$R \equiv \frac{\|\boldsymbol{\nabla} \ln E_{rad}\|}{\kappa_R \rho}, \qquad (4c)$$

where D_F is the diffusion coefficient, λ the flux limiter (see Section 5.1 below), κ_R the Rosseland mean, and R the "local radiation quantity" (see Paper I). Thus the radiative flux is assumed to be colinear with and opposite in direction to the gradient of radiation energy density.[7] In Equation (3), the combined cooling and heating or exchange term is

$$\Lambda \equiv c\kappa_P \rho\frac{4\pi S}{c} - c\kappa_E \rho E_{rad} \qquad (5a)$$

$$= c\kappa_P \rho(aT_{gas}^4 - E_{rad}). \qquad (5b)$$

We use the second line because we take the source function S to be the Planck function $B = \sigma T_{gas}^4/\pi$, with $4\sigma = ac$ (σ being the Stefan–Boltzmann constant and a and c the radiation constant and speed of light). This assumes local thermodynamic equilibrium. Our gray approximation suffices to make κ_P and κ_E, the Planck (blackbody-weighted) and E_{rad}-weighted mean opacities, respectively, be the same. Equations 3(a) and (b) are followed separately to prevent the Λ terms from canceling. This system states that the material (gas or dust, assumed here to have the same temperature) is losing energy at the rate $c\kappa_P \rho a T_{gas}^4$ but absorbing energy (photons) at the rate $c\kappa_E \rho E_{rad}$, and conversely for the radiation.

---

[7] In angularly resolved radiation transport methods, it is in fact possible for the radiation to flow *up* the E_{rad} gradient (McClarren & Drake 2010; Jiang et al. 2014). However, this can occur only for subcritical shocks and does not represent a large effect. It thus does not affect our work.
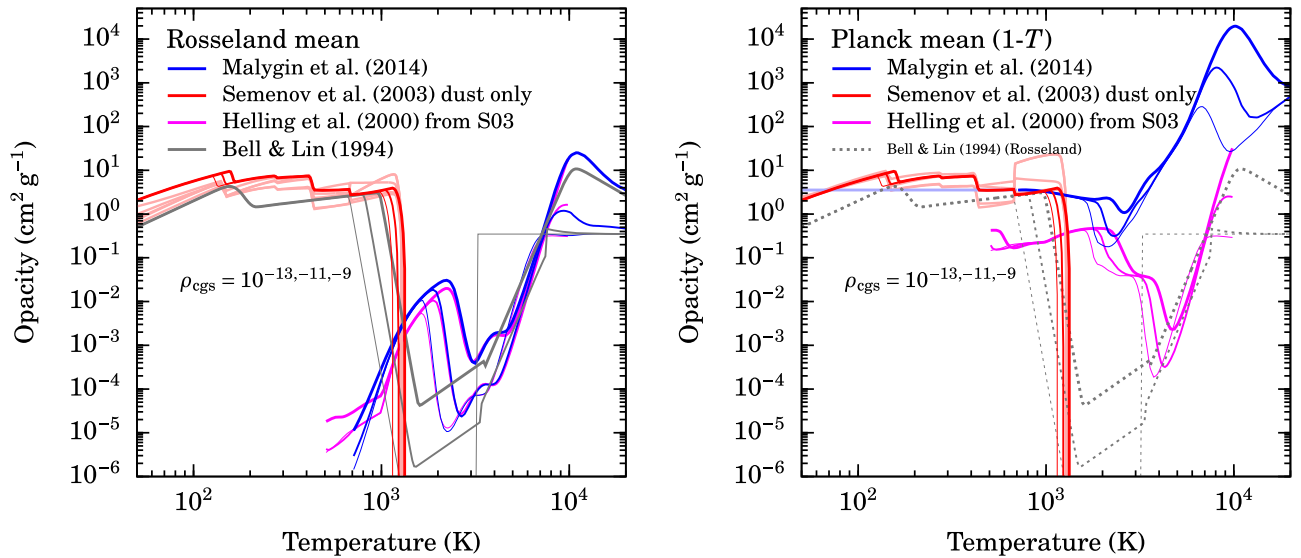
Figure 2. Rosseland (κ_R) and Planck (one-temperature; κ_P) mean opacities (left and right panels, respectively), from Malygin et al. ([2014](#)) for the gas and Semenov et al. ([2003](#)) for the dust. The total opacity is taken as the sum of the gas and dust contributions. Three densities are shown: $\rho = 10^{-13,-11,-9}$ g cm^{-3} (thin to thick lines). The Malygin et al. ([2014](#)) opacities are kept constant below the table limit of $T = 700$ K (pale blue ρ-independent lines in the right panel). Since Bell & Lin ([1994](#)) do not provide κ_P, their κ_R are displayed for comparison. Their curves reach down to $\kappa = 10^{-7}$–10^{-4} cm^2 g^{-1} (Paper I), roughly four orders of magnitude smaller than the Malygin et al. ([2014](#)) Planck values. We also display the Helling et al. ([2000](#)) κ_P opacities, which are also too low (Malygin et al. [2014](#)). For the Semenov et al. ([2003](#)) opacities, we show their "nrm.h.s" model (thick red lines). The other available "homogeneous" and "composite" models (thin pale red lines) are also shown at $\rho = 10^{-11}$ g cm^{-3}, with the curve sticking out mostly in the Planck mean being the five-layer composite model "nrm.c.5."

To solve the energy Equation [3](#)(b) in the radiation transport substep, the radiative flux F_{rad} is replaced by its expression from Equation ([4](#)), so that the FLD approach in fact does not naturally yield F_{rad} (nor thus the luminosity). While it is possible at a given time to calculate it from the output quantities $\rho(r)$, $E_{rad}(r)$, $\kappa_R(r)$ by Equation ([4](#)), this is approximate because in our implicit approach the diffusion coefficient D_F (Equation [4](#)(b)) is computed from the quantities at the current time while the ∇E_{rad} factor is written with E_{rad} at the following timestep. To avoid any numerical noise and inaccuracy, we therefore store D_F before the FLD step and combine it with E_{rad} after, thus exactly reconstructing the flux as it is effectively computed (albeit otherwise not explicitly). This was also done in Paper I but was not reported there.

We use the same outer boundary condition for E_{rad} as in Paper I, but verified that changing the outer temperature boundary condition (in particular to a Dirichlet boundary condition) does not affect the temperature or luminosity structure except at the largest radii.

3.3. Microphysics: Opacities

With respect to Paper I, we now always use the dust opacities of Semenov et al. ([2003](#)), taking by default their simplest model for the dust grains, the "normal homogeneous spheres" (`nrm_h_s`). It features more evaporation transitions than in Bell & Lin ([1994](#)), which we used originally. We slightly modified the opacity routine[8] to leave the evaporation of the most refractory component to be handled in the main code and to avoid adding the contribution from the Helling et al. ([2000](#)) gas opacities.

Instead, the gas opacity is provided by Malygin et al. ([2014](#)), and we take their one-temperature Planck mean, as opposed to

the 2-T Planck mean (see their Equation (4)). We found that it is crucial for numerical stability, especially toward higher constant μ and γ, to evaluate the single-temperature κ_P at the radiation temperature $T_{rad} \equiv (E_{rad}/a)^{1/4}$ and not at the gas temperature T_{gas}. Fortunately, it is also justified. Indeed, looking at $\kappa_P(T_{rad}, T_{gas})$ for fixed densities, one generally incurs a smaller mistake when using $\kappa_P \approx \kappa_P(T_{rad}, T_{rad})$ than with $\kappa_P \approx \kappa_P(T_{gas}, T_{gas})$. We also evaluate the dust opacities at T_{rad} but note that this barely makes a difference because we will find that the radiation and gas are always well coupled ($T_{gas} = T_{rad}$) in the region where the dust opacity matters ($T_{gas} \lesssim 1500$ K).

We recall that the Planck opacity is relevant for the coupling between dust/gas and radiation, whereas the Rosseland mean determines whether the radiation can stream freely or has to diffuse. This is discussed in more detail in Section [7.2](#).

The Planck opacity κ_P is shown in Figure [2](#) and is compared to the Rosseland mean κ_R. In the low-temperature, dust-dominated regime κ_P is similar to κ_R with $\kappa_P \sim \kappa_R \sim$ 1–10 cm^2 g^{-1}. For comparison, the different models of Semenov et al. ([2003](#)) are shown, with the exception of the porous models. We note that the fluffiness or porosity of dust aggregates during their growth remains an open question (see Cuzzi et al. [2014](#); Kataoka et al. [2014](#); Kirchschlager et al. [2019](#); Tazaki et al. [2019](#), and references in these works). In any case, the model curves of Semenov et al. ([2003](#)) for porous composite particles are not markedly different from the ones shown in Figure [2](#).

While the Rosseland mean opacity past dust evaporation (near $T \approx 1500$ K) drops to $\kappa_R \approx 10^{-2}$ cm^2 g^{-1} (see Figure 1 of Paper I), the Planck mean does not drop much below $\kappa_P \approx$ 1 cm^2 g^{-1} and even increases (between a few thousand to 10^4 K) to $\kappa_P = 10^2$–10^4 cm^2 g^{-1}, depending on the density.

Note that the Bell & Lin ([1994](#)) Rosseland mean opacities are three to six orders of magnitude (!) lower than the Planck average above the dust destruction temperature. This implies

---

[8] Original version available at http://www2.mpia-hd.mpg.de/home/henning/Dust_opacities/Opacities/opacities.html.
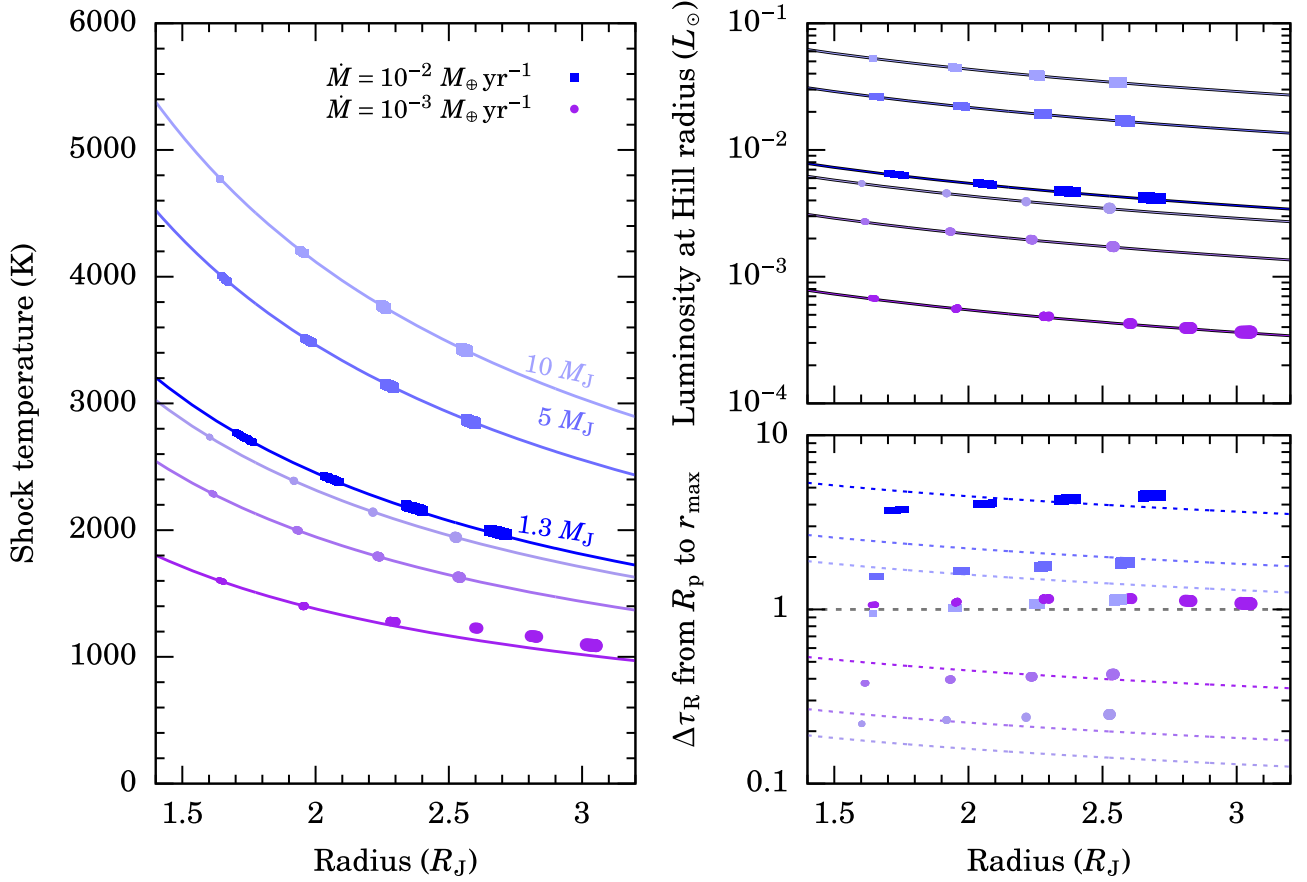
Figure 3. Shock properties in the perfect-gas case with ($\mu = 2.29$, $\gamma = 1.44$) and with tabulated opacities (Semenov et al. 2003; Malygin et al. 2014) for a grid of accretion rates $\dot{M} = 10^{-3}$–10^{-2} $M_\oplus$ yr^{-1} (color and symbol shape); masses $M_p = 1.3$, 5, 10 M_J (line saturation), and planet radii, i.e., shock positions $R_p \approx 1.5$–3 R_J. The symbol size scales with the position of the inner edge of the respective simulation box $r_{min} = 1.6$–2.9 R_J. Shown are *(left column)* the shock temperature T_{shock}; *(top right)* the luminosity at r_{max}, which is roughly the luminosity at the accretion radius $L(r_{max}) \approx L\left(\frac{1}{3}R_{Hill} \approx R_{acc}\right)$; and *(bottom right)* the Rosseland optical depth $\Delta\tau_R$ from R_p to r_{max}. Note that $L(R_{acc})$ depends on (μ, γ) (see Equations (42) and (45)). We compare in the temperature panel to Equation 6(b), i.e., with $\eta^{kin} = \Delta f_{red} = 1$; in the luminosity panel to Equation (8); and in the $\Delta\tau_R$ panel to the rough estimate Equation (9) with $\kappa_R = 1$ cm^2 g^{-1}, the gray long-dashed line highlighting $\Delta\tau_R \sim 1$.

that studies using nonequilibrium radiation transport with the Bell & Lin (1994) Rosseland mean as their Plank opacity are effectively assuming much less coupling between opacity carrier (dust or gas) and radiation. As Malygin et al. (2014) found out, a similar word of caution applies to the gas opacities of Helling et al. (2000), which are included in Semenov et al. (2003). Whether using these low opacities would actually lead to a strong disequilibrium between the matter and radiation will also depend on the local density and velocity, however, as briefly discussed in Section 7.2.

4. Grid of Simulations: Results and Analysis

We now present and discuss results for a grid of simulations for the macrophysical parameters

$$10^{-3} \leqslant \dot{M} \leqslant 10^{-2} \, M_\oplus \, \mathrm{yr}^{-1}$$
$$1.3 \leqslant M_p \leqslant 10 \, M_J$$
$$1.6 \lesssim R_p \lesssim 3 \, R_J.$$

We consider a mixture of molecular hydrogen and helium with helium mass fraction $Y = 0.25$, yielding $\mu = 2.29$ and $\gamma = 1.44$. At high temperatures, the hydrogen should dissociate (Szulágyi & Mordasini 2017), but we defer simulations that
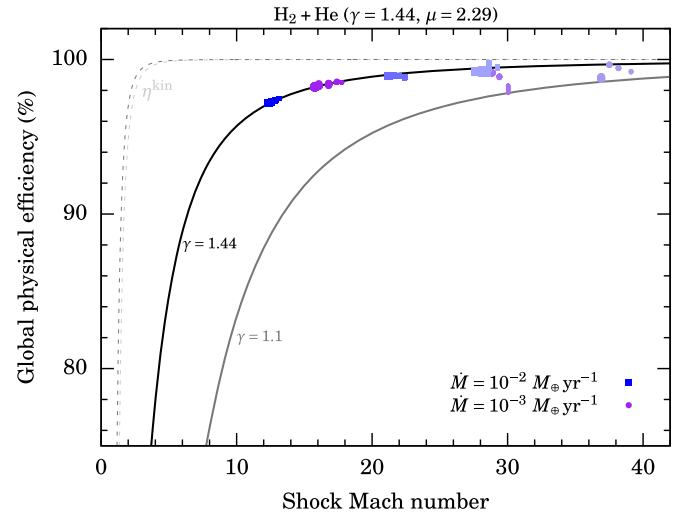

Figure 4. Global physical shock efficiency η^{phys} (Equation (10)) against the preshock Mach number $\mathcal{M}$ in the perfect-gas case with ($\mu = 2.29$, $\gamma = 1.44$) and with tabulated opacities (Semenov et al. 2003; Malygin et al. 2014) (grid of accretion rates, masses, and radii of Figure 3; see color, saturation, and shape meaning there). We compare to Equation (13) with $\gamma = 1.44$ (black) and $\gamma = 1.1$ for reference (gray), and also show η^{kin} (Equation (14)) for these two γ values (thin dashed gray lines). There is some noise in some simulations, but this is only cosmetic.
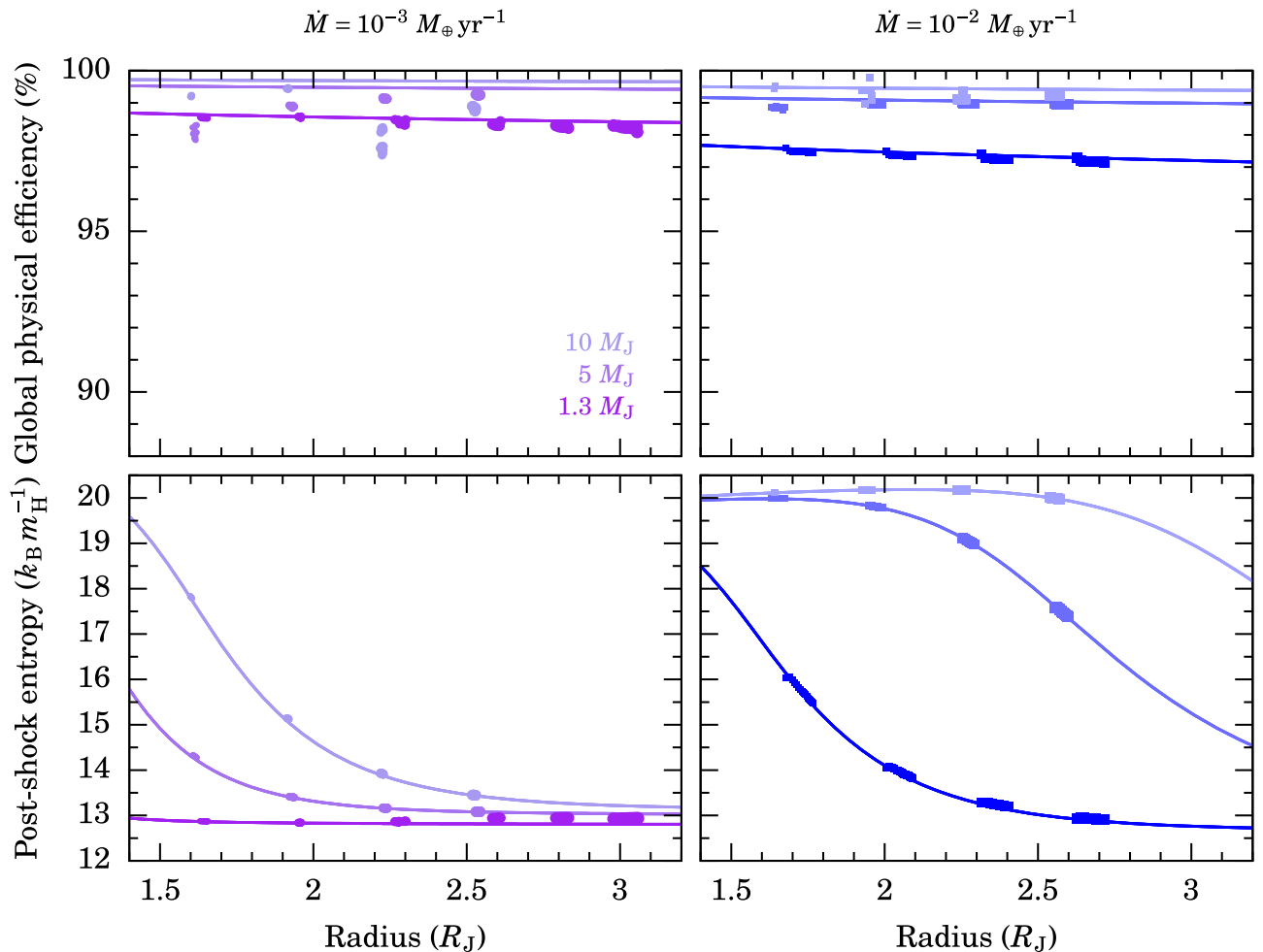
Figure 5. Top row: global physical efficiency η^{phys} for the simulations shown in Figure 3 using the same color and symbol coding. The theoretical curves (solid lines) use Equation (13) with $\mathcal{M} = v_{\mathrm{ff}}/c_{\mathrm{s}}$, with the sound speed c_{s} set by the temperature from Equation 6(b). Note the small vertical range. The deviations of the simulation data from the analytical expression at $\dot{M} = 10^{-3}\,M_{\oplus}\,\mathrm{yr}^{-1}$ are discussed in the text. Bottom row: postshock entropy $s(\dot{M}, M_{\mathrm{p}}, R_{\mathrm{p}})$ for the same simulations. The entropy is calculated with a full nonperfect EOS (Berardo et al. 2017), which formally is not self-consistent with the assumption of a perfect gas for the postshock temperature T_{shock} and pressure P_{ram} (dots: simulation results; lines: Equations 6(b) and (16)). However, because T_{shock} and P_{ram} should be independent of the EOS, the entropy values are probably realistic. The zero-point of the entropy (relevant only when comparing to other work) is discussed in the text.

take this into account to another paper in this series (G.-D. Marleau et al. 2019, in preparation).

The results are summarized in Figures 3–5 and discussed in the following: Figure 3 shows the resulting shock temperature as a function of the macrophysical parameters (Section 4.1), the luminosity at roughly the Hill radius (Section 4.2), and the optical depth to the Hill radius (Section 4.3), whereas Figure 4 shows the global physical efficiency as a function of the preshock Mach number (Section 4.4). Finally, in Figure 5 we display the efficiency as a function of the macrophysical parameters (Section 4.5) and the postshock entropy (Section 4.6).

Note that the grid is irregular in shock position because we considered the same r_{min} values for all masses and accretion rates but the shock moves at different rates dr_{shock}/dt; over the course of 2×10^7 s, which we use as the maximal simulation time because it is more than enough for the profiles to reach a quasi-steady state, the ranges of radial positions that the shock covers often do not overlap between different $(\dot{M}, M_{\mathrm{p}}, r_{\mathrm{min}})$. We added several simulations at higher $r_{\mathrm{min}} \leqslant 2.9\,R_{\mathrm{J}}$ for $(\dot{M} = 10^{-3}\,M_{\oplus}\,\mathrm{yr}^{-1}, M_{\mathrm{p}} = 1.3\,M_{\mathrm{J}})$.

4.1. Shock Temperature

For our choice of macrophysical parameters, the shock temperature is always above 1000 K. In Figure 3, simulations with a given $(\dot{M}, M_{\mathrm{p}})$ but different r_{min} (symbol size) are seen to lead to the same shock temperature at a given radius $r_{\mathrm{shock}} = R_{\mathrm{p}}$. This confirms that even though the postshock density structures differ, the shock properties do not depend on our placement of the inner boundary, thus supporting the robustness of our results. We have also verified that varying other numerical parameters such as the resolution or the tolerance in the FLD solver step (R. Kuiper et al. 2019, in preparation) does not modify the simulation outcomes.

An interesting result is that in all cases, the postshock gas and radiation (not shown) are in equilibrium, with $T_{\mathrm{gas}} = T_{\mathrm{rad}}$ to better than 1%, so that one can speak of a single temperature. The same applies to the preshock temperature. (For other choices of γ the equality is less strict but still within a few percent.) In Figure 3(a), the values we obtained are compared to the analytical shock estimate from Equation (27)

of Paper I

$$\sigma T_{\text{shock}}^4 = \frac{\eta^{\text{kin}}}{4\Delta f_{\text{red}}} \frac{\rho_{\text{ff}} v_{\text{shock}}^3}{2} \qquad (6\text{a})$$

$$\approx \frac{GM_{\text{p}}\dot{M}}{16\pi R_{\text{p}}^3}, \qquad (6\text{b})$$

where $\eta^{\text{kin}} \equiv \Delta F_{\text{rad}}/(0.5\rho v^3) \approx L_{\text{acc}}/(GM_{\text{p}}\dot{M}/R_{\text{p}})$ is the normalized jump in luminosity and $\Delta f_{\text{red}} \equiv f_{\text{red}}(r_{\text{shock}}^+) - f_{\text{red}}(r_{\text{shock}}^-)$ the jump in f_{red} at the shock. This equation is revisited in Section 5.3. The freefall density $\rho_{\text{ff}} = \dot{M}/(4\pi r^2 v_{\text{ff}})$ is evaluated ahead of the shock, with $v_{\text{ff}} = \sqrt{2GM_{\text{p}}/r}$ the approximate freefall velocity Paper I. The reduced flux

$$f_{\text{red}} \equiv F_{\text{rad}}/cE_{\text{rad}} \qquad (7)$$

is also termed the "streaming factor" (Kley 1989) because it indicates to what extent the radiation is freely streaming ($f_{\text{red}} \rightarrow 1$) or diffusing ($f_{\text{red}} \rightarrow 0$). In usual shock terminology, free-streaming regions are called "transmissive" (see Figure 8 of Vaytet et al. 2013b; Drake 2006; we recall in passing that Equation 6(a) is valid for $L_{\text{int}} \gtrsim L_{\text{acc}}$.) The simulations have preshock Mach numbers $\mathcal{M} \approx 7$–35 (Figure 4) and therefore $\eta^{\text{kin}} = 1$ (used in going from Equations 6(a) to (b)) because this is above $\mathcal{M} \approx 2.5$ (see the thin line in Figure 4; Paper I). Moreover, we find that $\Delta f_{\text{red}} \approx 1$ for a large part of the parameter space, i.e., the downstream regions are in the diffusion limit with $f_{\text{red}}(r_{\text{shock}}^-) \approx 0.03$–0.05 (equivalently, a flux limiter $\lambda \approx 1/3$), while the preshock region is in the free-streaming regime, with $f_{\text{red}}(r_{\text{shock}}^+) \approx 1$. Thus the shock is a "thick–thin" shock in the classification of Drake (2006).

As a consequence of this, Equation 6(b) holds very accurately for almost all simulations; we are almost always in the limit of Equation (28) of Paper I, discussed as Equation (33) below. There is an exception to this, namely for the lowest mass (1.3 M_{J}) at a low accretion rate (10^{-3} $M_{\oplus}$ yr^{-1}) and toward larger radii ($R_{\text{p}} \gtrsim 2.5$ R_{J}). In this case, the postshock temperature is higher than predicted from Equation 6(b) by $\Delta T \approx 50$ K. This is because f_{red} is lower ahead of the shock, with, e.g., $f_{\text{red}}^+ \equiv f_{\text{red}}(r_{\text{shock}}^+) = 0.65$ for the $T_{\text{shock}} \approx 1100$ K case. Indeed, because $F_{\text{rad}} \propto f_{\text{red}} T_{\text{rad}}^4$ and we find $T_{\text{gas}} = T_{\text{rad}}$, a lower f_{red} at a location requires a higher temperature for the same radiation flux (equal to the kinetic energy flux) to flow through that location. As discussed in Paper I, this smaller f_{red} can also be pictured as a slower effective speed of light, so that E_{rad} must increase so as to have the same $F_{\text{rad}} = c_{\text{eff}} E_{\text{rad}}$. We return to these points in Section 5.3 and show that another effect is also at play. Note, however, that this is the gas temperature but not the *effective* temperature, with only the latter setting the spectral shape.

4.2. Luminosity at the Hill Sphere

Figure 3(b) shows the luminosity at the outer edge of the grid, which is very nearly equal to the luminosity at the Hill sphere, as we show in Section 6.1.2. The Mach numbers we find here are all $\mathcal{M} > 2.5$, so that essentially the entire kinetic energy is converted into radiation (see the pale gray curve in Figure 4). Because for the specific choice of ($\mu = 2.29$, $\gamma = 1.44$), the decrease in L from the shock to R_{Hill} is insignificant (see Section 6.1), the entire

kinetic energy is transformed into visible radiation, according to the usual expression for the shock luminosity,

$$L_{\text{acc}} = \frac{GM_{\text{p}}\dot{M}}{R_{\text{p}}}. \qquad (8)$$

This equation is shown as solid lines and seen to match very well (note that the symbols are almost smaller than the line), even though we neglected the finite "accretion radius" R_{acc}. This radius is much larger than the planet radius, however, because we are considering the detached phase during giant planet formation (Mordasini et al. 2012b).

We also produced a grid with ($\mu = 1.1$, $\gamma = 1.1$) (not shown), which increases the contrast with the present situation. One example is discussed in Section 6.1 below. Over the grid, however, the shock temperatures were the same, as one would expect from Equation (6) because they do not explicitly depend on the EOS. The situation could be different for an ideal but nonperfect EOS, but due to the potential sink of energy (dissociation and ionization). As for the luminosity at the Hill radius, it was different from the $\mu = 1.23$ case and was lower by at most $\approx 10\%$ compared to the immediate shock upstream luminosity. The luminosity profile is discussed in Section 6.1.

4.3. Optical Depth of the Infalling Gas

Figure 3(c) displays the Rosseland mean optical depth from the shock to the outer edge of the computational domain, $\Delta\tau_{\text{R}} = -\int_{r_{\text{max}}}^{r_{\text{shock}}} \rho\kappa_{\text{R}} \, dr$. Especially for the lower masses, the contribution from the outer layers is actually significant despite their low density, and $\Delta\tau_{\text{R}}$ does depend on the choice of the domain size (here, $r_{\text{max}} = 0.7R_{\text{acc}}$ as in Paper I). We find that $\Delta\tau_{\text{R}} \approx 0.2$–5, increasing with accretion rate and decreasing with mass. This is qualitatively as expected from Equation (24) of Paper I

$$\Delta\tau_{\text{R}} \sim 3\left(\frac{\kappa_{\text{R}}}{1 \text{ cm}^2 \text{ g}^{-1}}\right)\left(\frac{\dot{M}}{10^{-2} \, M_{\oplus} \text{ yr}^{-1}}\right)$$
$$\times \sqrt{\left(\frac{1 \, M_{\text{J}}}{M_{\text{p}}}\right)\left(\frac{2 \, R_{\text{J}}}{r_{\text{shock}}}\right)}, \qquad (9)$$

shown as dotted lines in Figure 3(c). The agreement with the nominal models is not too rough (to at worse 1 dex) considering that we took a constant $\kappa_{\text{R}} = 1$ cm^2 g^{-1} in Equation (9) in this estimate for all simulations. In the radial profiles, the maximum value of the actual $\kappa_{\text{R}}(r)$ is near 7(3) cm^2 g^{-1} for $\dot{M} = 10^{-3}$ (10^{-2}) $M_{\oplus}$ yr^{-1}. However, contrary to what was explained in Paper I, what is relevant is the *immediate* preshock opacity, as we show in Section 5.

The significance of Figure 3(c) can only be appreciated in conjunction with panels (a) and (b). It shows that the total optical depth, at least up to moderate depths of $\Delta\tau_{\text{R}} \sim 10$, does not set the shock temperature or the shock luminosity (which is nearly identical to the Hill-radius luminosity in the present case). In fact, the deviations of T_{shock} from Equation (6) do not occur at the highest optical depths. (What causes these deviations is explained in Section 5.) Furthermore, when, as is often the case, the layers between the $\Delta\tau_{\text{R}} \sim 1$ surface and the shock are not sufficiently diffusive ($f_{\text{red}} \lesssim 0.1$), it does not hold that $T_{\text{shock}}^4 \approx \frac{3}{4}\left(\Delta\tau_{\text{R}}(r) + \frac{2}{3}\right)T_{\text{eff}}^4$, where T_{eff} is the

temperature at the radius where $\Delta\tau_R = 2/3$, the photosphere, and where $\Delta\tau_R(r) = -\int_{r_{max}}^{r} \rho\kappa_R\,dr'$ is the optical depth measured from the outer radius inward. The temperature rise from the photosphere to the shock is much higher because the optical depth increases more slowly when the radiation is less diffusive, i.e., when $d\tau/dr = \kappa_R\rho$ is small.

Finally, we note that there is nothing special about the $\Delta\tau_R \sim 1$ surface. As Figure 3(c) shows, most simulations at $\dot{M} = 10^{-3}\,M_\oplus\,\mathrm{yr}^{-1}$ remain optically thin or barely optically thick above the shock, but their temperature structure (not shown) is qualitatively identical to cases with an optically thick accretion flow. In any case, $\Delta\tau_R$ is not well defined because it depends on the outer integration radius. We return to considerations of shock temperature in Section 5.3.

4.4. Shock Efficiency against Mach Number

When calculating a planet structure for given $(\dot{M}, M_p, R_p)$, only the postshock (P_{post}, T_{shock}) point is used in an approach equivalent to the one used in mesa by Berardo et al. (2017) and Berardo & Cumming (2017). This yields the density ρ; from this and $\dot{M}$, the boundary condition on the velocity v and thus the luminosity profile $L(r)$ in the postshock region follow (Berardo et al. 2017). When only the global energetics are followed (see the review in Section 2.1 of Berardo et al. 2017), we argued in Paper I that one should use η^{phys} and not η^{kin}.

We show in Figure 4 the "global physical efficiency" η^{phys} of the shock against the preshock Mach number. The quantity η^{phys} is measured as (Paper I, their Equation (18))

$$\eta^{phys} \equiv \frac{\dot{E}(r_{max}) - \dot{E}(r_{shock}^-)}{\dot{E}(r_{max})}, \qquad (10)$$

where r_{shock}^- is immediately downstream of the shock. The material-energy flow rate is defined as

$$\dot{E}(r) \equiv -|\dot{M}|[e_{kin}(r) + h(r) + \Delta\Phi(r, r_{shock})], \qquad (11)$$

where $e_{kin} = \frac{1}{2}v^2$, e_{int}, and $h = e_{int} + P/\rho$ are the kinetic energy, internal energy density, and the enthalpy per unit mass, respectively, and Φ is the external potential. The $\Delta\Phi$ term in Equation (11) accounts for the work done by the potential on the gas down to the shock, with the potential difference from r_0 to r given by

$$\Delta\Phi(r, r_0) = -GM_p\left(\frac{1}{r} - \frac{1}{r_0}\right). \qquad (12)$$

We found that for all simulations here, using the tenth cell below the shock as the postshock location was a robust prescription. The shock itself was identified by the $dv/dr < 0$ and $\Delta P/\min(P) > 5$ criterion in Appendix B of Mignone et al. (2012).

The efficiency η^{phys} measured from Equation (10) is compared in Figure 4 as a function of the Mach number to the analytical result in the isothermal limit (Paper I, their Equation (36)),

$$\eta_{isoth}^{phys} = \eta_{isoth}^{kin} \times \left(1 + \frac{2}{\gamma - 1}\frac{1}{\mathcal{M}^2}\right)^{-1} \qquad (13a)$$

$$= \frac{(\gamma^2\mathcal{M}^4 - 1)(\gamma - 1)}{\gamma^2\mathcal{M}^2[(\gamma - 1)\mathcal{M}^2 + 2]}, \qquad (13b)$$

with the isothermal "kinetic efficiency" given by (Commerçon et al. 2011a)

$$\eta_{isoth}^{kin} = 1 - \frac{1}{\gamma^2\mathcal{M}^4}. \qquad (14)$$

This definition was derived from energy conservation for the 1-T case but it is also meaningful here because shocks are isothermal in the radiation temperature, and we find that the gas and radiation are tightly coupled.

As expected, we find essentially perfect agreement between the measured (Equation (10)) and the theoretical (Equation (13)) efficiencies. This reflects both energy conservation by our radiation-hydrodynamical code and the isothermality—i.e., super-criticality—of the shock.

We also computed the kinetic efficiency,

$$\eta^{kin} \equiv \frac{\Delta F_{rad}}{\frac{1}{2}\rho_+v_+^3}, \qquad (15)$$

where ΔF_{rad} is the jump in radiative flux at the shock and ρ_+ and v_+ are the density and velocity upstream of the shock. This measured η^{kin} was found to match Equation (14). As mentioned above, because $\mathcal{M} \gtrsim 2.5$ and the shock is isothermal, we have $\eta^{kin} \approx 100\%$. Locally at the shock, the whole incoming kinetic energy is thus converted into radiation.

4.5. Shock Efficiency Against Formation Parameters

Figure 5 shows the global physical efficiency η^{phys} but now as an explicit function of the (possibly observable, macro-physical) formation parameters $(\dot{M}, M_p, R_p)$. The efficiencies range from 97% at high accretion rate to almost 100% at low $\dot{M}$, increasing both with decreasing radius and increasing mass. The precise range depends on the assumed EOS, but qualitatively our results should be robust. Typically, in core-accretion formation, the radius decreases as the mass grows in the detached phase.[9] Because the gas accretion onto a planet usually slows down with time, at least in the single-embryo-per-disk simulations of Mordasini et al. (2012b), our simulations clearly suggest that the efficiency η^{phys} increases over time. Thus, the accretion of the outer layers is associated with less energy recycling (Paper I) in the accretion flow, and a greater net fraction of the kinetic energy escapes the system.

However, as discussed in Mordasini (2013), there could be a self-amplifying memory effect: an η^{phys} that is small early after detachment should lead to the accretion of "hot" (high-entropy) material into the planet. If the planetary accretion timescale is much shorter than its global cooling timescale—i.e., $t_{acc} \equiv M_p/\dot{M} \ll t_{KH} \equiv GM_p^2/(R_pL_p)$, where t_{acc} and t_{KH} are the accretion and Kelvin–Helmholtz timescales, respectively, with L the luminosity at the radiative–convective boundary (Berardo et al. 2017)—, a large planet radius should ensue. This large radius would in turn keep η^{phys} small, so that the planet would always remain in a regime where it is accreting rather high-entropy material. Ultimately, this would lead to a hot (or at least warm) start. This scenario should be tested with dedicated evolutionary simulations coupling the shock efficiency self-consistently with the interior structure. It might also

be instructive to compare this with accretion in the context of star formation, where a similar phenomenon is seen (Hosokawa & Omukai 2009; Hosokawa et al. 2013; Kuiper & Yorke 2013). Care should be taken to distinguish in the analysis the *local* accretion and cooling times of the material immediately below the accretion shock from the global ones t_{acc} and t_{KH} (i.e., for the planet as a whole).

4.6. Postshock Entropy

Our detailed calculations of the accretion shock are meant to serve as outer boundary conditions for calculating the structure of accreting planets as in Mordasini et al. (2012b), Berardo et al. (2017), Berardo & Cumming (2017), and Cumming et al. (2018). Because these planet structure calculations always use a full EOS including chemical reactions (dissociation and ionization), we use this to compute the entropy corresponding to the shock temperatures and pressures we obtained above. This is formally *not* self-consistent given that we assumed a perfect EOS for the shock simulations. However, because T_{shock} should be independent of the EOS, as we argue in Section 6.1, the entropy values are possibly realistic. In any event, they will serve as a comparison point for simulations with a realistic EOS (G.-D. Marleau et al. 2019, in preparation).

To calculate the entropy, we can use the ideal-gas form $P = \rho/(\mu m_H)k_B T$ (but with variable μ) because degeneracy effects start being relevant only at a conservative limit of $\rho \sim 10^{-2}$ g cm^{-3} (see Figure 1 of SCvH), several orders of magnitude above even the highest postshock densities $\rho_{post} \propto \rho_{pre}\mathcal{M}^2$, with $\rho_{pre} \sim 10^{-13}$–10^{-10} g cm^{-3} (see Figure 4 of Paper I) and $\mathcal{M} \ll 100$, so that $\rho_{post} \ll 10^{-6}$ g cm^{-3}. We use the Saha equation and Sackur–Tetrode formula as implemented[10] in Berardo et al. (2017). The entropy zero-point (see Appendix B of Marleau & Cumming 2014 and footnote 2 of Mordasini et al. 2017) is the same as in the published version of SCvH and `mesa` (Paxton et al. 2011, 2013, 2015, 2018), and thus the entropy values reported here are higher by $(1 - Y)\ln 2 = 0.52 \, k_B \, m_H^{-1}$, where $Y = 0.25$ is the helium mass fraction, than those in, e.g., Mordasini et al. (2017). The zero-point of the entropy is not physically meaningful but does have to be taken into account when comparing entropies from different works.

These effective postshock entropies s_{post} are shown in Figure 5. For the range of shock positions $r_{shock} \approx 1.5$–$3 \, R_J$ and masses $M_p = 1.3$–$10 \, M_J$ shown, the entropies for $\dot{M} = 10^{-3} \, M_\oplus$ yr^{-1} are mostly around $s_{post} \approx 12$–14 but go up to $s_{post} \approx 19$ (dropping, also in the following, the usual units of $k_B \, m_H^{-1}$ for clarity). For $\dot{M} = 10^{-2} \, M_\oplus$ yr^{-1}, the whole range $s_{post} \approx 13$–20 is covered. These values are high compared to the postformation entropy of planets, which is at most around 10–$14 \, k_B \, m_H^{-1}$ according to current, though not definitive, predictions (Mordasini 2013; Berardo & Cumming 2017; Berardo et al. 2017; Mordasini et al. 2017). However, we caution and emphasize that this postshock entropy is not the same as the entropy below the postshock settling layer; this latter quantity is most likely the one most relevant in setting the entropy of the planet as it accretes.

---

[10] See https://github.com/andrewcumming/gasgiant.

Before calculating the (non-self-consistent) postshock entropy analytically, we briefly discuss the ram pressure,

$$P_{ram} = \rho v_{ff}^2 = \frac{\dot{M}}{4\pi R_p^2}v_{ff} = \frac{\sqrt{2G}}{4\pi}\frac{M_p^{1/2}\dot{M}}{R_p^{5/2}}. \quad (16)$$

We inserted the expressions for freefall from infinity and find that Equation (16) holds very well for all simulations, even for those for which $\Delta f_{red} \neq 1$. At high shock temperatures, the small pressure buildup ahead of the shock slows the gas down slightly, making Equation (16) less accurate by at most 3.5% for the range of parameters shown. Given the relatively weak (logarithmic, with a small prefactor) dependence of the entropy $s(P, T)$ on P, outside of dissociation or ionization regions, this will not be an important source of inaccuracy. The ram pressure varies from $P_{ram} \approx 10^{-4}$ bar to 0.2 bar for the range of parameters discussed here.

We compare the postshock entropies s_{post} in Figure 5 based on the actual T to s_{post} using as input $T = T_{shock}$ from Equation 6(b), i.e., taking $\eta^{kin} = \Delta f_{red} = 1$ for all simulations. The match is very good, which reflects the overall good match of temperature, on which the entropy depends only logarithmically.

5. Analytics of the Temperature ahead of and at the Shock

As we show in Figure 9, the temperature profile upstream of the shock shows variations that appear to be related to variations in opacity. This modifies the temperature at the outer edge of the accretion flow (i.e., the local nebula temperature) compared to what a naive extrapolation $T(r) = T_{shock}(r_{shock}/r)^{-1/2}$ would predict. Also, and even more importantly, the temperature at the shock is obviously a key outcome of our simulations. The usual expression for the shock temperature, with our modification of a factor $(1/4)^{1/4}$ (Equation (6)), provides in general a very good estimate. However, we have seen in Figure 3 that there can be small deviations. We now turn to the task of understanding both the temperature profile in the accretion flow and the shock temperature by analytical means. We also discuss the link between the reduced flux and the Rosseland opacity.

5.1. Temperature Profile in the Accretion Flow

To derive the slope of the temperature throughout the infalling gas, let us begin with the general relationships

$$acT_{rad}^4 = \frac{L}{4\pi r^2}\frac{1}{f_{red}} \quad (17)$$

$$f_{red} = R\lambda(R), \quad (18)$$

with $aT_{rad}^4 \equiv E_{rad}$. The first equation is nothing but a rewriting of the definition of f_{red}, and the second follows from Equation (17) and the definition of the radiation quantity R, given by

$$R \equiv \frac{1}{\kappa_R \rho}\left|\frac{d \ln E_{rad}}{dr}\right| \quad (19)$$

in spherical symmetry. (In this section we use the symbol "d" instead of "∂" because of time independence.) It is equal to the ratio of the photon mean free path to the "E_{rad} scale height"
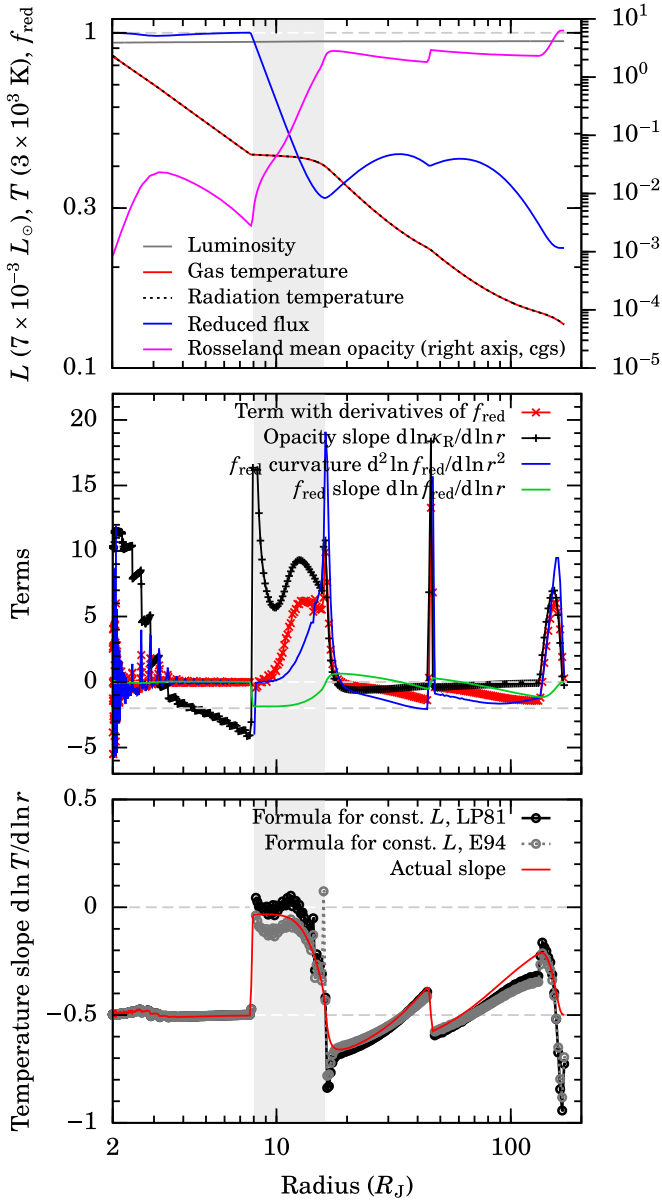
Figure 6. Top panel: normalized luminosity, temperatures (gas and radiation), reduced flux (against the left axis), and opacity κ_R (against the outer right axis) for the nominal case presented in Figure 9. Note the logarithmic scale. The region with a temperature flattening ($r = 8$–$16\,R_J$) due to dust destruction is highlighted. Middle panel: first two curves: different terms in the brackets in Equation (28) (see legend). Some of the factors are plotted individually (blue and green lines). Bottom panel: temperature slope obtained from Equation (28) for two flux limiters (black and gray lines; in both cases the same simulations are used, with λ changing only in the formula). This is compared to the exact result (red line).

(Paper I). Taking the derivative of Equation (17) yields

$$\frac{d \ln T_{\rm rad}^4}{d \ln r} = -2 + \frac{d \ln L}{d \ln r} - \frac{d \ln f_{\rm red}}{d \ln r}. \qquad (20)$$

The last term, by Equation (18), is

$$\frac{d \ln f_{\rm red}}{d \ln r} = \frac{d \ln R}{d \ln r}\left(1 + \frac{d \ln \lambda}{d \ln R}\right). \qquad (21)$$

These expressions are exact and general. We now proceed to expand the last equation.

By the definition of R, the first factor in Equation (21) is

$$\frac{d \ln R}{d \ln r} = \frac{d}{d \ln r}\left(\ln\left[\frac{d \ln T_{\rm rad}^4}{d \ln r}\right] - \ln[\kappa_R \rho r]\right) \qquad (22)$$

because $E_{\rm rad} = aT_{\rm rad}^4$. Inserting recursively Equation (20) into Equation (22) is likely not fruitful as it generates derivatives of $f_{\rm red}$ of ever-higher order. However, it will prove instructive to perform this once. In full generality, this yields

$$\frac{d \ln R}{d \ln r} = \frac{d^2_{(\ln r)^2} \ln L - d^2_{(\ln r)^2} \ln f_{\rm red}}{-2 + d_{\ln r} \ln L - d_{\ln r} \ln f_{\rm red}} - \frac{d \ln \kappa_R}{d \ln r} + \frac{1}{2}, \qquad (23)$$

where $d^n_{x^n} f(x) \equiv d^n f(x)/dx^n$. For this derivation we have made use of the fact that $\rho \propto r^{-3/2}$ in the accretion flow.

The second factor in Equation (21) depends only on the choice of the flux limiter and can be computed easily independently of a simulation. If one takes the flux limiter used in Ensman (1994),

$$\lambda(R) = \frac{1}{3 + R}, \qquad (24)$$

one obtains for the derivative term the simple expression

$$1 + \frac{d \ln \lambda}{d \ln R} = 3\lambda. \qquad (25)$$

Note that this flux limiter is actually not physical (Levermore 1984), but it recovers the correct limits of free-streaming and diffusion (see Paper I). When the rational approximation of the Levermore & Pomraning (1981) flux limiter

$$\lambda(R) = \frac{2 + R}{6 + 3R + R^2}, \qquad (26)$$

which we take by default in this work, is used instead, the result is

$$1 + \frac{d \ln \lambda}{d \ln R} = 1 - \frac{R^2(R + 4)}{(2 + R)(6 + 3R + R^2)}. \qquad (27)$$

For $R \ll 2$ (the diffusion limit), this function (the right-hand side) is equal to 3λ. In the other limit of $R \gg 2$, it converges to simply λ; in any case, it remains roughly proportional to the flux limiter λ, a fact we shall use in the discussion below.

Combining Equations (20), (21), (23), and (25), we obtain

$$\frac{d \ln T}{d \ln r} \approx -\frac{1}{2} + \frac{3\lambda(R)}{4}\left[\frac{d^2_{(\ln r)^2} \ln f_{\rm red}}{2 + d_{\ln r} \ln f_{\rm red}} - \frac{d \ln \kappa_R}{d \ln r} + \frac{1}{2}\right] \qquad (28)$$

in the limit of a radially constant luminosity (in the sense that $|d \ln L/d \ln r| \ll 2$, which is the case here as shown below). The temperature here was written as T because we find that $T_{\rm gas} = T_{\rm rad}$; if the gas and radiation are not coupled, T should be taken to refer to $T_{\rm rad}$ only. We used Equation (25) because it makes it explicit that the second term on the right-hand side of Equation (28) is (in general roughly) proportional to the flux limiter $\lambda(R)$. While at least in this form, Equation (28) is not predictive because $f_{\rm red}(r)$ is needed for its derivatives, it does exhibit the link between the temperature and the opacity slopes, as we now discuss.

Looking in detail at Equation (28), we see that the first term on the right-hand side corresponds to the result that $T \propto r^{-1/2}$ for a radially constant luminosity. It seems likely that this term will dominate in the free-streaming (often termed "optically thin") regime because then λ (and thus the second term) goes to zero.

For the temperature slope to differ significantly from $-1/2$, it is sufficient for either the opacity slope or the term with derivatives of $f_{\rm red}$ to be large, and necessary for the radiation to be sufficiently diffusive (λ not too small).

The second term of Equation (28) is interesting: it relates the local slope of the opacity to that of the temperature. In the free-streaming regime, the flux limiter λ goes to zero and thus also the second term in Equation (28) because it is multiplied by λ). Therefore, even strong variations of $\kappa_{\rm R}$ with radius will only minorly affect the temperature structure; this is as expected for the limit of infinite optical mean free path, in which the radiation does not interact with the opacity carrier. In the other limiting case of diffusion, $\lambda \approx 1/3$ and the opacity variations are important. The evaporation of dust as the material moves in leads to a large $d \ln \kappa_{\rm R} / d \ln r$, and if λ is not too small, this will be able to slow the decrease of the temperature outward.

Moreover, it does not seem necessary that the radiation be free streaming ($f_{\rm red} \to 1$) in order to have $T \propto r^{-1/2}$, which is usually associated with free streaming. If $\kappa_{\rm R}$ is constant with radius and (as perhaps a consequence) $f_{\rm red}$ is sufficiently constant, and λ has an intermediate value (e.g., $\lambda \sim 0.1$), the $-1/2$ term in Equation (28) can dominate.

We show in the top panel of Figure 6 the luminosity, temperature, reduced flux, and opacity on logarithmic scales for the nominal case shown in Figure 9. Indeed, the luminosity is effectively radially constant.

The middle panel of Figure 6 shows the terms on the right-hand side of Equation (28) and parts thereof. In the free-streaming region at $r = 2$–$8\,R_{\rm J}$, the first and second derivatives of $f_{\rm red}$ are nearly zero, and the strong values of the opacity slope do not bring T away from an $r^{-1/2}$ scaling because the radiation is nearly free-streaming: $f_{\rm red} \approx 1$ (see top panel), so that $\lambda \approx 0$. In the flat temperature part at $r = 8$–$16\,R_{\rm J}$ (shaded region), the opacity slope term dominates, but the term with the derivatives of $f_{\rm red}$ is similar in magnitude, with their signed sum dominating the $-1/2$ term. The result, along with a lower $f_{\rm red}$ (i.e., higher λ), is a different (namely, almost zero) temperature slope. At $r > 16\,R_{\rm J}$, the radiation remains somewhat diffusive with $f_{\rm red} \sim 0.3$, but the opacity is nearly constant. The temperature slope is therefore set by the leading $-1/2$ term as well as the two other terms in the brackets and the factor of $\approx 3\lambda$ (depending on the flux limiter model). The net result is that the $-1/2$ dominates.

The slope from Equation (28) is shown in the bottom panel of Figure 6 and compared to the actual value. The agreement is excellent, which mainly confirms the approximation $dL/dr \approx 0$ because the equation is otherwise exact for a freefall density profile. The choice of the flux limiter barely makes a difference.

Note finally that Equations (19) and (20) imply that when the ratio $L1/f_{\rm red}$ is radially constant, the radiation quantity R is given by

$$R = \frac{2}{\kappa_{\rm R}\rho r} \qquad (\text{constant } L/f_{\rm red}). \qquad (29)$$

This had been derived in Paper I, above their Equation (25).

This analysis provides an approximate analytical understanding of the link between the opacity and the temperature. What is less clear from this derivation is how much the geometry accurately reflects the realistic transport of radiation, even within the gray approximation, and to what extent it depends on the approximations (e.g., concerning the angular distribution of the specific intensity) inherent to moments-based methods such as FLD. Nevertheless, it might prove insightful to attempt a similar derivation using M1 radiation transport (e.g., González et al. 2007; Hanawa & Audit 2014).

5.2. Link between Reduced Flux and Opacity

Figure 6 suggests that there is a relationship between the reduced flux $f_{\rm red}$ and the Rosseland mean opacity $\kappa_{\rm R}$. Defining the logarithmic slope

$$\beta \equiv \frac{d \ln (L/f_{\rm red})}{d \ln r}, \qquad (30)$$

this relationship can be obtained by combining Equations (17)–(19) to yield

$$\frac{1}{f_{\rm red}} = 1 + \frac{3}{|2 - \beta|}\kappa_{\rm R}\rho r \qquad (31a)$$

$$= 1 + \frac{3}{2}\kappa_{\rm R}\rho r \qquad (\text{constant} L/f_{\rm red}), \qquad (31b)$$

which holds anywhere in the flow. This generalizes Equation (25) in Paper I. We used λ from Equation (24), but it is trivial to repeat the derivation for another flux limiter.

Equation (31) explains why $f_{\rm red}$ drops in the dust destruction region in Figure 6 (gray band there): the opacity increases such that $\kappa_{\rm R}\rho r \gtrsim 1$, thereby leading to a drop in $f_{\rm red}$. Physically, this has the intuitive explanation that the radiation becomes less freely streaming and starts to diffuse. In the dust destruction region, $\beta \approx 1.87$ (and relatively constant) due to the outward decreasing $f_{\rm red}$. From Equation 31(a) this implies that $1/f_{\rm red}$ will be larger, i.e., $f_{\rm red}$ smaller, than predicted by Equation 31(b), but the trend is the same. Quantitiatively, this works well in this example, but to obtain the exact value of $f_{\rm red}$, one would have to use the Levermore & Pomraning (1981) flux limiter because this was chosen for the simulations. Thus, Equation (31) explains the sudden drop of $f_{\rm red}$ where the opacity suddenly increases to become important in the sense of $\kappa_{\rm R}\rho r \gtrsim 1$.

5.3. Shock Temperature

5.3.1. Calculation Setup

We now turn to explaining the shock temperatures found in Figure 3, in particular the points that deviate from Equation 6(b). We recall that this temperature more precisely refers to the radiation temperature $T_{\rm rad}$, should it ever be found to differ from $T_{\rm gas}$, which is not the case here, however.

Looking at the results of Section 4.1 again, there is a tight anticorrelation (not shown) between $f_{\rm red}$ and $\kappa_{\rm R}\rho r$ both evaluated immediately upstream of the shock. Empirically across our grid of models, $\beta(r_{\rm shock}{}^{+}) \sim -0.1$ typically, which in absolute value is $\ll 2$. Therefore, the tight relationship comes from Equation 31(b). Thus while in general, $\beta(r_{\rm shock}{}^{+})$ is not known but could perhaps be estimated, in the following analysis we restrict ourselves to $\beta(r_{\rm shock}{}^{+}) \ll 2$ and consequently use $R(r_{\rm shock}{}^{+}) = 2/\kappa_{\rm R}\rho_{\rm ff}R_{\rm p}$ at the shock (Equation (29)).
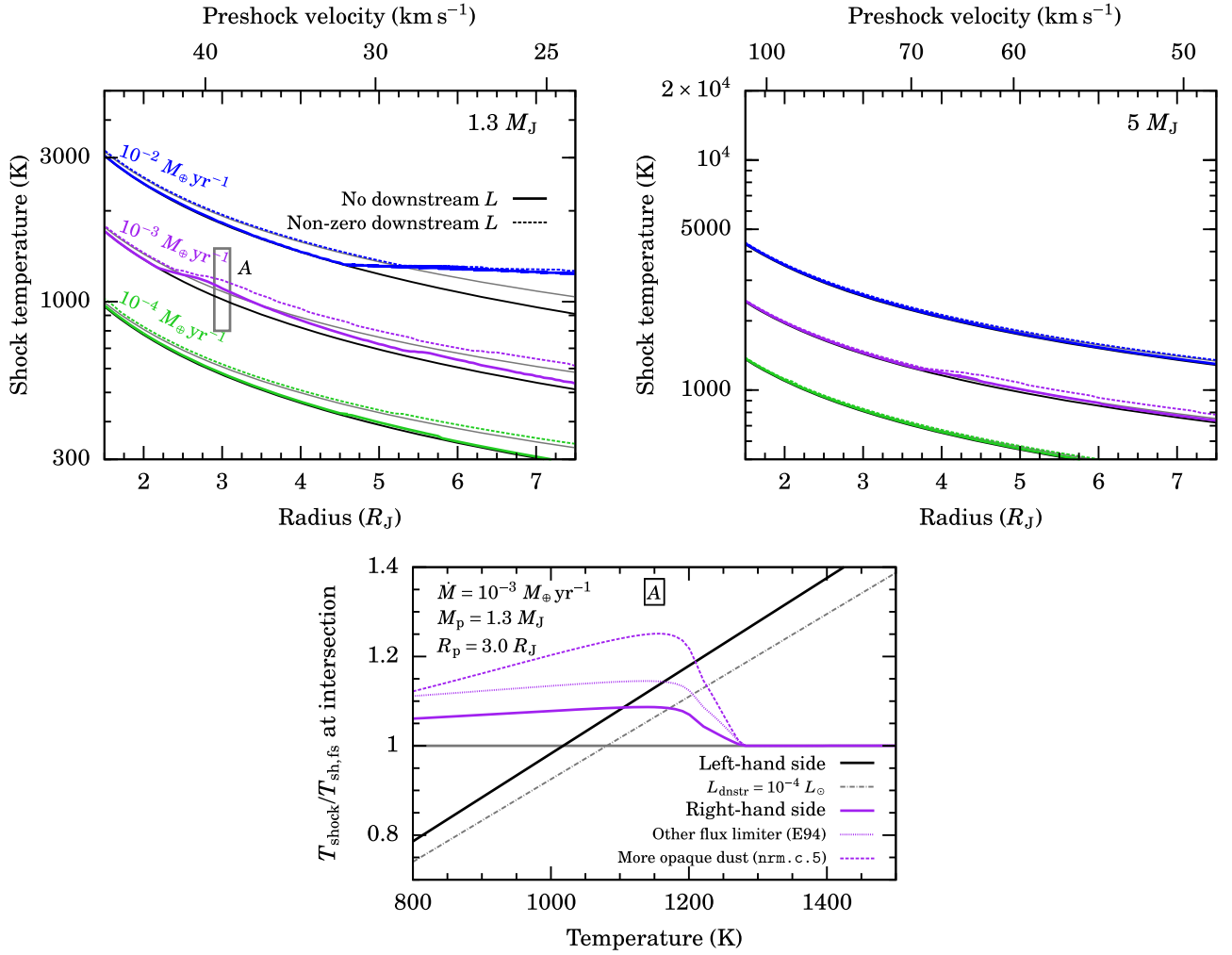
Marleau, Mordasini, & Kuiper

Figure 7. Top row: analytical shock temperature T_{shock} taking upstream opacity effects into account, obtained by implicitly solving Equation (35). We use accretion rates of $\dot{M} = 10^{-4}$ to $10^{-2}\,M_\oplus\,\text{yr}^{-1}$ (bottom to top). Planet masses of $1.3\,M_{\text{J}}$ (left panel) and $5\,M_{\text{J}}$ (right panel) are shown. Both $L_{\text{dnstr}} = 0$ (*full lines*) and $\log_{10}(L_{\text{dnstr}}/L_\odot) = \log_{10}(\dot{M}/M_\oplus\,\text{yr}^{-1}) - 1$ (*dashed lines*) are shown. The "free-streaming solution" (Equation (33)) is shown by solid lines (*black and gray, respectively*). Along the top axes, the corresponding freefall velocities are indicated. An example for label A in the left panel is shown in the bottom row. Bottom row: graphical solution of Equation (35) for $\dot{M} = 10^{-3}$ when $M_{\text{p}} = 1.3\,M_{\text{J}}$ and $R_{\text{p}} = 3\,R_{\text{J}}$. We plot the fourth root of the left- and right-hand sides. We vary (see legend) L_{dnstr} (nominal: $L_{\text{dnstr}} = 0$), the flux limiter (nominal: LP81), and the opacity model (nominal: nrm.h.s), which leads to different solutions. The denominator of the quantity on the y-axis, $T_{\text{sh,fs}}$, is evaluated at $L_{\text{dnstr}} = 0$. The shock temperature is given by the intersection of the left- and right-hand sides.

With this, Equation 6(a) can be rewritten as

$$\sigma T_{\text{shock}}^4 = \frac{L_{\text{dnstr}} + \eta^{\text{kin}}(T_{\text{shock}})\frac{GM_{\text{p}}\dot{M}}{R_{\text{p}}}}{f_{\text{red}}^+(T_{\text{shock}})16\pi R_{\text{p}}^2} \qquad (32a)$$

$$\approx \left(1 + \frac{3}{2}\kappa_{\text{R}}(T_{\text{shock}})\rho_{\text{ff}}R_{\text{p}}\right)\frac{L_{\text{dnstr}} + \frac{GM_{\text{p}}\dot{M}}{R_{\text{p}}}}{16\pi R_{\text{p}}^2}, \qquad (32b)$$

which is an implicit equation for T_{shock}. The second line is valid when the resulting $\mathcal{M} \gtrsim 2.5$ (so that $\eta^{\text{kin}} \approx 1$), which should be verified a posteriori, and was written for the Ensman (1994) flux limiter through Equation (31). The downstream luminosity L_{dnstr} is the sum of the luminosity coming from the deep interior and of the compression luminosity: $L_{\text{dnstr}} = L_{\text{int}} + L_{\text{compr}}$. While L_{compr} might depend on T_{shock}, we effectively absorb this dependency into L_{int}, treated as a free parameter. Still, the generalization $L_{\text{dnstr}} \to L_{\text{dnstr}}(T_{\text{shock}})$ could be readily

made. With these assumptions, in Equation 32(b) the shock temperature enters on the right-hand side only through the opacity.

In the 100% efficiency limit, the shock temperature that solves Equation 32(b) thus has the limiting cases

$$T_{\text{sh,fs}} \equiv T_{\text{shock}}(\kappa_{\text{R}}\rho R_{\text{p}} \ll 1) \qquad (33a)$$

$$= \ell^{1/4}\left(\frac{G}{16\pi\sigma}\right)^{1/4}\frac{M_{\text{p}}^{1/4}\dot{M}^{1/4}}{R_{\text{p}}^{3/4}} \qquad (33b)$$

$$= 2315\,\text{K}\,\ell^{1/4}\left(\frac{R_{\text{p}}}{2\,R_{\text{J}}}\right)^{-3/4}$$

$$\times \left(\frac{\dot{M}}{10^{-2}\,M_\oplus\,\text{yr}^{-1}}\right)^{1/4}\left(\frac{M_{\text{p}}}{1\,M_{\text{J}}}\right)^{1/4}, \qquad (33c)$$

$$T_{\text{sh,diff}} \equiv T_{\text{shock}}(\kappa_{\text{R}}\rho R_{\text{p}} \gg 1) \qquad (34a)$$

$$= \ell^{1/4}\left(\frac{3\sqrt{G}}{128\sqrt{2}\,\pi^2\sigma}\right)^{1/4}\frac{\dot{M}^{1/2}\kappa_{\text{R}}^{1/4}M_{\text{p}}^{1/8}}{R_{\text{p}}^{7/8}} \qquad (34b)$$
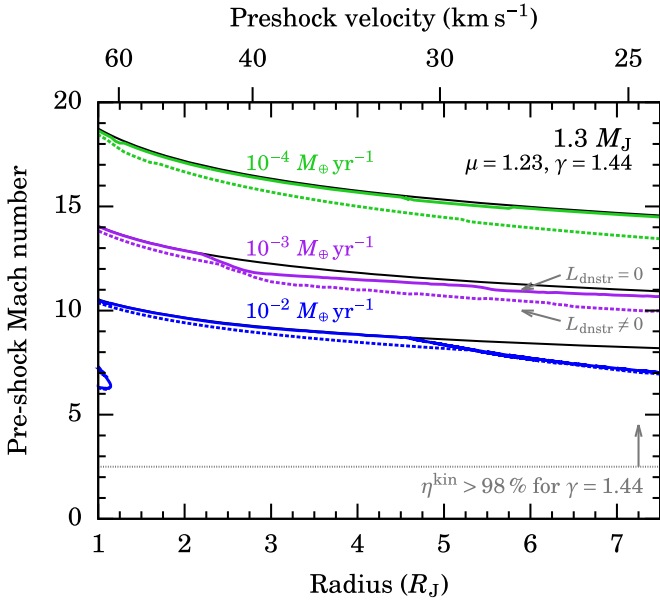
Figure 8. Analytical preshock Mach number. The mass is $M_p = 1.3\,M_J$ and the radius and accretion rate are varied. We use $\mu = 1.23$ (different from our nominal case) and $\gamma = 1.44$ to obtain a rough lower bound on the Mach number and thus also on η^{kin}. As in Figure 7, colored solid (short dashed) lines are for $L_{dnstr} = 0$ ($L_{dnstr} \neq 0$), using the implicit shock temperature from Equation 32(b). The limiting case of $\Delta f_{red} = 1$ (which implies simultaneously $L_{dnstr} = 0$ and the free-streaming limit for the shock temperature; Equation (38)) is also shown (solid black lines). The value $\mathscr{M} = 2.5$ is highlighted because above this, η^{kin} is essentially 100% (*dotted line*).

$$= 3220\,\text{K}\,\ell^{1/4}\left(\frac{R_p}{2\,R_J}\right)^{-7/8}\left(\frac{\kappa_R}{1\,\text{cm}^2\,\text{g}^{-1}}\right)^{1/4}$$

$$\times\left(\frac{\dot{M}}{10^{-2}\,M_\oplus\,\text{yr}^{-1}}\right)^{1/2}\left(\frac{M_p}{1\,M_J}\right)^{1/8}, \qquad (34\text{c})$$

with $\ell = 1 + L_{dnstr}/L_{acc,max}$, without needing to assume that $L_{dnstr}/L_{acc,max}$ is small. We defined $T_{sh,fs}$ as the "free-streaming shock temperature" given by Equation 6(b), but now generalized to include a downstream luminosity L_{dnstr} (we consider $L_{dnstr} = 0$ in this work). Similarly, $T_{sh,diff}$ is the "diffusive shock temperature," which obtains when the preshock material is diffusive. The maximum accretion luminosity is $L_{acc,max} = GM_p\dot{M}/R_p$, with the actual luminosity at the shock $L_{acc} = \eta^{kin}L_{acc,max}$ (Paper I). The opacity κ_R appearing in the expressions for $T_{sh,diff}$ is either the constant opacity or less trivially, the value satisfying Equation 32(b), as detailed below. Equation 34(c) should replace Equation 28(b) of Paper I because the prefactor there was inexact and the exponent of the R_p factor was missing a minus sign. Equations 34(b) and (c) were written to leading order in the quantity $\kappa_R\rho_{ff}r_{shock}$, in which case they are also independent of the flux limiter. Note that if L_{dnstr} were to dominate $L_{acc,max}$ ($\ell \gg 1$), the functional dependence of the shock temperature on the various parameters would be different from what Equations (33) and (34) naively suggest.

As an example, for the ($\gamma = 1.1$, $\kappa = 1\,\text{cm}^2\,\text{g}^{-1}$) simulation in Figure 2 of Paper I, Equation (34) predicts $T_{sh,fs} \approx 3600$ K, which is close to the actual shock temperature 3500 K. This is

satisfying, especially given that there $\kappa_R\rho R_p = 2.3$, which is not entirely $\gg 1$, and that the Levermore & Pomraning (1981) flux limiter had been used and not the Ensman (1994) one as for Equations 34(b) and (c), which makes a difference in this transition regime between free streaming and diffusion.

In general, we solve Equation 32(b) by writing it as

$$\left(\frac{T_{shock}}{T_{sh,fs}}\right)^4 = \begin{cases} 1 + \frac{3}{2}x & \text{(E94)} \\ \left(1 + \frac{3}{2}x + \frac{3}{2}x^2\right)/(1+x) & \text{(LP81)} \end{cases}, \quad (35)$$

with

$$x(T_{shock}) \equiv \kappa_R(T_{shock})\rho_{ff}R_p. \qquad (36)$$

The first and second versions of the right-hand side of Equation (35) hold for the flux limiters of Ensman (1994, E94) and Levermore & Pomraning (1981, LP81), respectively. The equation is solved by root finding, simply starting slightly below $T = T_{sh,fs}$ and stepping up in temperature to find an intersection of the two sides of Equation (35).

5.3.2. Semianalytical Shock Temperature Solutions

In Figure 7 we display the shock temperature as a function of planet radius according to Equation (35). We consider $M_p = 1.3$ and $5\,M_J$, take $\dot{M} = 10^{-4,-3,-2}\,M_\oplus\,\text{yr}^{-1}$, and vary R_p from 1 to about $7\,R_J$, but truncating at lower R_p for the lowest accretion rate. The downstream luminosity is taken to be zero or smaller than but not entirely negligible compared to the accretion luminosity, $\log_{10}(L_{dnstr}/L_\odot) = \log_{10}(\dot{M}/M_\oplus\,\text{yr}^{-1}) - 1$ for definiteness. For reference, the corresponding preshock (freefall) velocity is indicated on the top axis. The solution is also compared to the free-streaming shock temperature $T_{sh,fs}$ (Equation (33)).

Figure 7 reveals that opacity effects can alter the shock temperature only for a relatively small range of parameters. Specifically, for $\dot{M} \sim 10^{-3}$–$10^{-2}\,M_\oplus\,\text{yr}^{-1}$, planets of low mass ($M_p \lesssim 3\,M_J$) with moderate to large radii ($R_p \approx 3$–$10\,R_J$) could have their T_{shock} increased by up to tens of percent, by a few 100 K. This might be important especially for a nonzero L_{int}, leading to a higher shock temperature than naively expected.

5.3.3. Regimes of the Shock Temperature

To understand these results graphically, we show in the bottom row of Figure 7 the fourth root of the left- and right-hand sides of Equation (35). We see that the points that deviate in Figure 3 can do so for two reasons. First of all, a high constant (temperature- and density-independent) opacity will increase the shock temperature by reducing the effective speed of light ahead of the shock. The threshold for this is $\kappa_R\rho_{ff}R_p \sim 1$, as mentioned above, and an example is for ($\dot{M} = 10^{-3}\,M_\oplus\,\text{yr}^{-1}$, $M_p = 1.3\,M_J$, $R_p = 3\,R_J$), labeled "A," where the opacity of the most refractory dust component leads to a higher shock temperature than $T_{sh,fs} = 1000$ K: $T_{shock} \approx 1080$ K for the nominal dust model and $T_{shock} \approx 1200$ K for the curve sticking out most in Figure 2. Second of all, the case of *nonconstant* high ($\kappa_R\rho_{ff}R_p \gtrsim 1$) opacities opens up the possibility of multiple solutions.

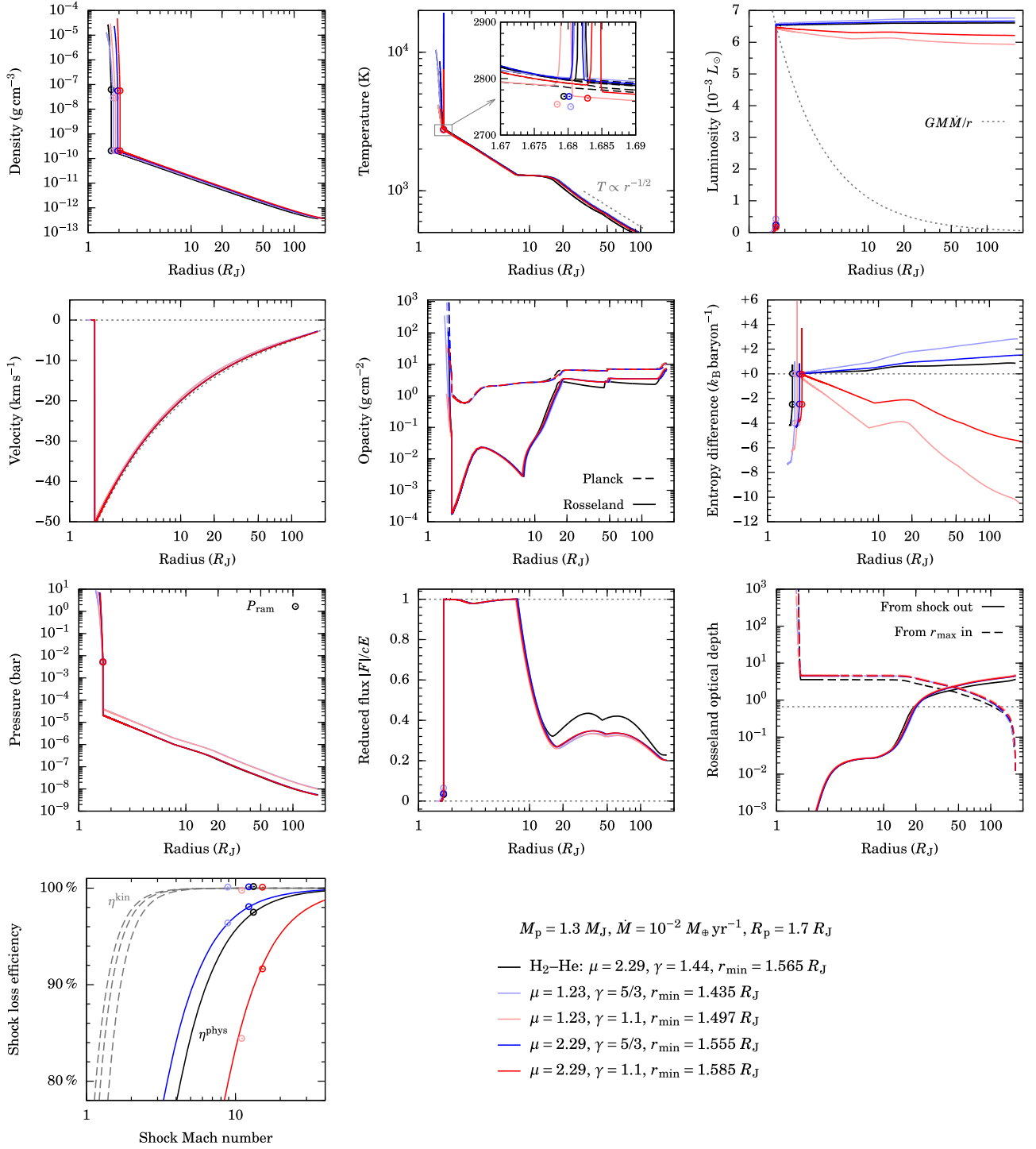**Figure 9.** Accretion and shock profiles (see axis labels) using a perfect equation of state with different mean molecular weights μ and ratios of specific heat γ (see legend). The black line corresponds to the nominal case of an H_2–He mixture. The Malygin et al. (2014) and Semenov et al. (2003) opacities are used. The simulations differ only in μ, γ, and the inner edge of the computational domain r_{min} (see legend), the latter chosen to have the shocks coincide at a time $t = 5 \times 10^7$ s after the start of accretion at $t = 0$. All but the first profile in the density and entropy-difference panels are shifted horizontally for legibility. Gray dotted lines highlight values of 0, 1, or 2/3 in the v, f_{red}, S and $\Delta\tau$ panels, as appropriate. Circles in the temperature panel and its inset show the estimate from Equation 6(a), whereas in the density, luminosity, pressure, and f_{red} panels they highlight the postshock conditions and in part the preshock conditions. In the $\eta^{phys}(\mathcal{M})$ panel on the bottom left, the solid (dashed) curves show the physical (kinetic) efficiency for $\gamma = 5/3$, 1.44, 1.1 (top to bottom) compared to the simulation results (circles).

If $\kappa_R \rho R_p \ll 1$ at the free-streaming shock temperature $T_{sh,fs}$, it is necessary and sufficient for the opacity slope

$$\alpha_\kappa \equiv \left(\frac{\partial \ln \kappa_R}{\partial \ln T}\right)_\rho \tag{37}$$

to satisfy $\alpha_\kappa > \alpha_\kappa^{crit} = 1$ at higher temperatures and for a sufficient T range in order to have one high-T solution. A drop of α_κ below α_κ^{crit} at a higher temperature will lead to a third solution. The stronger the slopes, the closer these higher-T solutions will be to $T_{sh,fs}$.

If on the other hand $\kappa_R \rho R_p \gtrsim 1$ at $T_{\rm sh,fs}$ (i.e., the preshock gas would be diffusive already if it were at that temperature), $T_{\rm sh,fs}$ will not be a solution. Provided the opacity slope $\alpha_\kappa < 1$ at some higher temperature, there will only be a single[11] solution at high temperature. Again, the stronger the slopes $|\alpha_\kappa|$ in the increasing and decreasing parts, the closer the solution will be to $T_{\rm sh,fs}$.

If $\kappa_R \rho R_p \gtrsim 1$ at $T_{\rm sh,fs}$ and α_κ remained >1 at higher temperatures, however, there would formally be no solution: try it as it may by increasing its temperature, the shock would not be able to radiate away the kinetic energy. It is not clear, however, whether in this case we would still find a Mach number such that $\eta^{\rm kin} = 1$, or if the model otherwise breaks down. Fortunately, for gas mixtures as considered here, α_κ does drop again, so that the situation does not arise.

Qualitatively, these results do not depend much on different model settings. Including a low downstream luminosity (coming from compression, an interior luminosity, or both) does not significantly change the shock temperature(s) of Figure 7. Changing the opacity (the dust model or, at higher temperature, the abundance of water; Malygin et al. 2014) or the flux limiter also has a clear but limited effect.

5.3.4. Mach Number

Within the restriction of negligible $L_{\rm dnstr}$, the Mach number $\mathcal{M}$ increases with increasing M_p or $1/R_p$, but, perhaps counterintuitively, decreases with increasing accretion rate. Using Equation (6), the Mach number is

$$\mathcal{M} = 2\left(\frac{G^3 \pi \sigma \Delta f_{\rm red}}{\eta^{\rm kin}}\right)^{1/8} \sqrt{\frac{\mu m_H}{\gamma k_B}} \left(\frac{M_p^3}{\dot{M} R_p}\right)^{1/8} \quad (38a)$$

$$= 30\left(\frac{M_p}{1.3 M_J}\right)^{3/8} \left(\frac{\mu}{2.29}\right)^{1/2} \left(\frac{\gamma}{1.44}\right)^{-1/2}$$
$$\times \left(\frac{\dot{M}}{10^{-2} M_\oplus {\rm yr}^{-1}}\right)^{-1/8} \left(\frac{R_p}{1.5 R_J}\right)^{-1/8}, \quad (38b)$$

where we took $\eta^{\rm kin} = 1$ and $\Delta f_{\rm red} = 1$ for the second expression. Thus the Mach number depends only moderately on the mass ($\mathcal{M} \propto M_p^{3/8 \approx 0.4}$) and accretion rate (given that the latter ranges over several orders of magnitude) and barely on the radius.

We show in Figure 8 the preshock Mach number obtained from Equation 32(b) with $\mu = 1.23$, and also plot Equation (38) for reference. Mach numbers increase with decreasing accretion rate, reaching $\mathcal{M} \sim 30$ (in particular at higher masses, not shown) for $\dot{M} = 10^{-4}\, M_\oplus\, {\rm yr}^{-1}$. The Mach number at $T_{\rm sh,fs}$, given by Equation (38), provides an upper bound but $\mathcal{M}$ still remains securely above $\mathcal{M} \approx 2.5$. There, $\eta^{\rm kin}$ is near 100%, which justifies our approximation a posteriori. Also, taking $L_{\rm dnstr}$ not large (see Figure 8) but nonzero barely changes these results.

---

[11] In the case that the opacity shows several nonmonotonicities at higher temperatures, the number of roots is of course different and the discussion would need to be adapted. This is presumably the case at the iron opacity "bump" at $\log T \approx 5.3$ (Iglesias et al. 1992; Jiang et al. 2015), and in principle also for a very metal-rich gas.

5.3.5. Discussion of the Analytical Shock Temperature

The preceding analysis has shown that for an isothermal radiative shock with negligible downstream luminosity, the shock temperature is determined by the conditions immediately upstream. There can be small to very important deviations from the free-streaming result $T_{\rm sh,fs}$. These occur either because of the dust contribution to the opacity (at low temperature) or because of the high opacity and high preshock density at high temperature and accretion rates. Nevertheless, the $T_{\rm sh,fs}$ solution remains valid for a large part of parameter space.

Interestingly, our derivations do not depend explicitly on the EOS, specifically on the choice of and (non-)constancy of μ and γ across or ahead of the shock. Thus the expressions (32)–(34) for the shock temperature could also apply to the case of a general EOS. This is should certainly be the case for $(\dot{M}, M_p, R_p)$ combinations for which the pre- and postshock points have the same γ and μ values. It might also hold more generally, but this will be investigated in a subsequent article.

Finally, note that the importance of a shock temperature increased with respect to $T_{\rm sh,fs}$ for lower planet masses and larger radii than shown here, as might be relevant during the early stages of detachment (runaway accretion), will have to be assessed with separate formation calculations as in Berardo et al. (2017).

6. Importance of the EOS and Opacity

Next we verify the robustness of our results by varying different parts of the microphysics that go into our simulations. This also gives us occasion to show global profiles of the accretion flow; we had restricted ourselves in Figure 2 of Paper I to the vicinity of the shock.

6.1. Dependence of Preshock-region Quantities on the EOS

While the use of an ideal but nonperfect EOS is deferred to a later article, we study in this section the importance of the constant μ and γ. For conciseness, we refer to a particular (μ, γ) combination as an EOS.

Figure 9 shows the profiles for the four extreme combinations (μ, γ), where $\mu = 1.23$ (atomic) or $\mu = 2.29$ (molecular), and $\gamma = 1.1$ (occurring for dissociation or ionization) or $\gamma = 5/3$ (monatomic, no dissociation or ionization) together with the nominal case ($\mu = 2.29$, $\gamma = 1.44$), i.e., for a perfect-gas H_2–He mixture. The density in the accretion flow being set by mass conservation, it is independent of the EOS, but the jump across the shock scales as $\Delta \rho \propto \mu$. The pressure in the accretion flow does scale as $P \propto 1/\mu$, but being a dynamical quantity, the ram pressure (i.e., the postshock pressure) is the same in all cases. While this might be counterintuitive, the shock temperature (see inset) is also independent of (μ, γ), which was to be expected from the analytical estimates of the shock temperature because the microphysical parameters do not enter anywhere. The opacities κ_R and κ_P are the same here because we use the same tables in all cases (computed using an nonperfect EOS) while the opacity is fundamentally a function of temperature and density (but not mean molecular weight).

6.1.1. Entropy

One of the quantities that change with the EOS is the entropy calculated with the chosen (μ, γ). Note that it differs from the entropy that would be obtained with nonperfect EOS shock

simulations. This (μ, γ)-dependent entropy is given in general (but for constant (μ, γ), i.e., outside of chemical reactions such as conversion of ortho- to parahydrogen, dissociation, or ionization) by

$$s = s_0 + \frac{\gamma}{\gamma - 1} \frac{\ln(10)}{\mu} \log_{10} \frac{T}{T_0} - \frac{\ln(10)}{\mu} \log_{10} \frac{P}{P_0}, \quad (39)$$

where s_0 is a constant, and T_0 and P_0 are an arbitrary reference temperature and pressure, respectively. The form is similar as a function of (P, ρ) (e.g., Rafikov 2016).

The radial profile of the entropy given by Equation (39) is shown in Figure 9 for various EOS. We plot in fact the entropy difference with respect to the preshock location because we are interested in the radial profiles of s for the individual (μ, γ) cases. It increases outward for $\gamma = 5/3$ because it is greater than the critical value of 4/3 (Section 3.3.2 of Paper I) but decreases for $\gamma = 1.1$ (because then $\gamma < 4/3$) outward in the accretion flow. Convection is not expected there because of the supersonic motion, however.

6.1.2. Luminosity

Another difference between the various EOS is in the luminosity profile, as Figure 9 shows. We now proceed to explain it. The luminosity L varies throughout the accretion flow by an amount that depends on the EOS, *not* directly on the optical depth. This perhaps surprising statement can be derived from considering the steady-state (time-independent) version of the evolution equation for the total energy (so that the $\pm\Lambda$ terms cancel even in nonequilibrium radiation transport; Equation (3)) and writing the gravity field term as a potential:

$$\frac{dL}{dr} = |\dot{M}| \left(\frac{dh}{dr} + \frac{d}{dr} \left[\frac{1}{2}v^2 - \frac{GM_p}{r} \right] \right) \quad (40a)$$

$$= |\dot{M}| \left(\frac{dh}{dr} - \frac{1}{\rho} \frac{dP}{dr} \right) \quad (40b)$$

$$= |\dot{M}| \left(\frac{de_{int}}{dr} + P \frac{d(1/\rho)}{dr} \right) \quad (40c)$$

$$= |\dot{M}| T \frac{ds}{dr}, \quad (40d)$$

where $h = H/\rho = e_{int} + P/\rho$ is the specific enthalpy per mass and is given by $h = \gamma/(\gamma - 1) k_B T/(\mu m_H)$ for a perfect EOS. Only Equation 40(a) was derived in Paper I. It did not require identifying the gas and radiation temperatures with each other, leaving the derivation valid also for 2-T radiation transport. Equation 40(b) is obtained from $\dot{M} = 4\pi r^2 \rho v$ (Equation 1(a)) and the time-independent momentum equation (Equation 1(b)). Equation 40(d) follows from the first law of thermodynamics,

$$T ds = de_{int} + P d\left(\frac{1}{\rho}\right), \quad (41)$$

with the entropy s here not normalized by $k_B\, m_H^{-1}$. Note that Equation (40) both above and below the shock. In the pre-shock region, it is the small deviation of the velocity from a freefall profile that makes $dL/dr \propto T ds/dr$ and not $\propto dh/dr$.

In Paper I, we had argued that the radial non-constancy (over $\sim$ Hill-sphere scales) of the luminosity can be understood from the enthalpy profile when the second term in Equation 40(a) is negligible. While this is formally true, Equation (40) provides a

more complete derivation that reveals that the relevant quantity is the *entropy*, without requiring restrictions on any term. Thus the radial luminosity profile is set not directly by the optical depth. Nevertheless, the analysis in Section 5.1 has shown that there is a link between the local opacity and its slope on the one hand and the temperature (and thus the entropy) profile on the other.

In the case of a perfect EOS, Equation 40(d) becomes

$$\frac{dL}{dr} = \frac{|\dot{M}|}{\gamma - 1} \frac{k_B T}{\mu m_H} \left[\frac{d \ln T}{dr} - (\gamma - 1) \frac{d \ln \rho}{dr} \right] \quad (42a)$$

$$= \frac{k_B |\dot{M}|}{\mu m_H} \frac{T}{r} \left[\frac{1}{\gamma - 1} \frac{d \ln T}{d \ln r} + \frac{3}{2} \right], \quad (42b)$$

where the second line holds for a freefall density profile. Because the factor T/r in Equation 42(b) decreases outward, it is the layers closest to the shock that contribute most to the change in L between r_{shock} and r_{max}, at least for a constant logarithmic temperature slope. Equation (42) reveals that, all other things being equal, the change in luminosity from the shock to the Hill sphere will be more important as γ tends to 1 (i.e., more isothermal), or for smaller mean molecular weight μ. The choice of γ can change the sign of dL/dr, whereas μ cannot.

In fact, an estimate for the change in luminosity between the shock and a given distance in the flow, in particular the accretion radius, can be derived by using the constant-(L/f_{red}) temperature profile (see Equation (20))

$$T(r) = T_{shock} \left(\frac{r_{shock}}{r} \right)^{-1/2}, \quad (43)$$

where T_{shock} is the shock temperature, which by Equation (35) can be higher than the free-streaming temperature. (Note that $T \propto r^{-1/2}$ can hold not only for free-streaming.) In Figure 6(c) or Figure 9, the $T(r)$ profiles are rarely steeper than Equation (43), so that it will provide an upper bound. Inserting Equation (43) in Equation (42) yields

$$\frac{dL_{(43)}}{dr} = -\frac{|\dot{M}|}{\gamma - 1} \frac{k_B T_{shock}}{\mu m_H} \frac{4 - 3\gamma}{2R_p} \left(\frac{r}{R_p} \right)^{3/2}, \quad (44)$$

using the subscript "(43)" on L to recall that a temperature profile given by Equation (43) was assumed. Thus, the change (drop or increase) in $L_{(43)}$ between R_p and R_{acc}, neglecting terms of order $\sqrt{R_p/R_{acc}} \ll 1$, is given by

$$\Delta L_{(43)} = \int_{R_p}^{R_{acc}} \frac{dL}{dr} = \frac{3\gamma - 4}{\gamma - 1} \frac{k_B T_{shock} |\dot{M}|}{\mu m_H}, \quad (45)$$

with the luminosity reaching the local circumstellar disk (the nebula) equal to

$$L(R_{acc}) \approx L_{int} + L_{acc} + \Delta L_{(43)}. \quad (46)$$

Equation (45) is more general than Equation (32) in Paper I. In the usual limit $R_{acc} \gg R_p$, the luminosity change $\Delta L_{(43)}$ is thus independent of R_{acc}, and thus also of $k_{Lissauer} = 1/3$ (as we assume here) for the accretion radius $R_{acc} \approx k_{Lissauer} R_{Hill}$. For $\gamma > 4/3$, the luminosity increases outward ($\Delta L_{(43)} > 0$), whereas for $\gamma < 4/3$ there is a decrease in luminosity ($\Delta L_{(43)} < 0$).
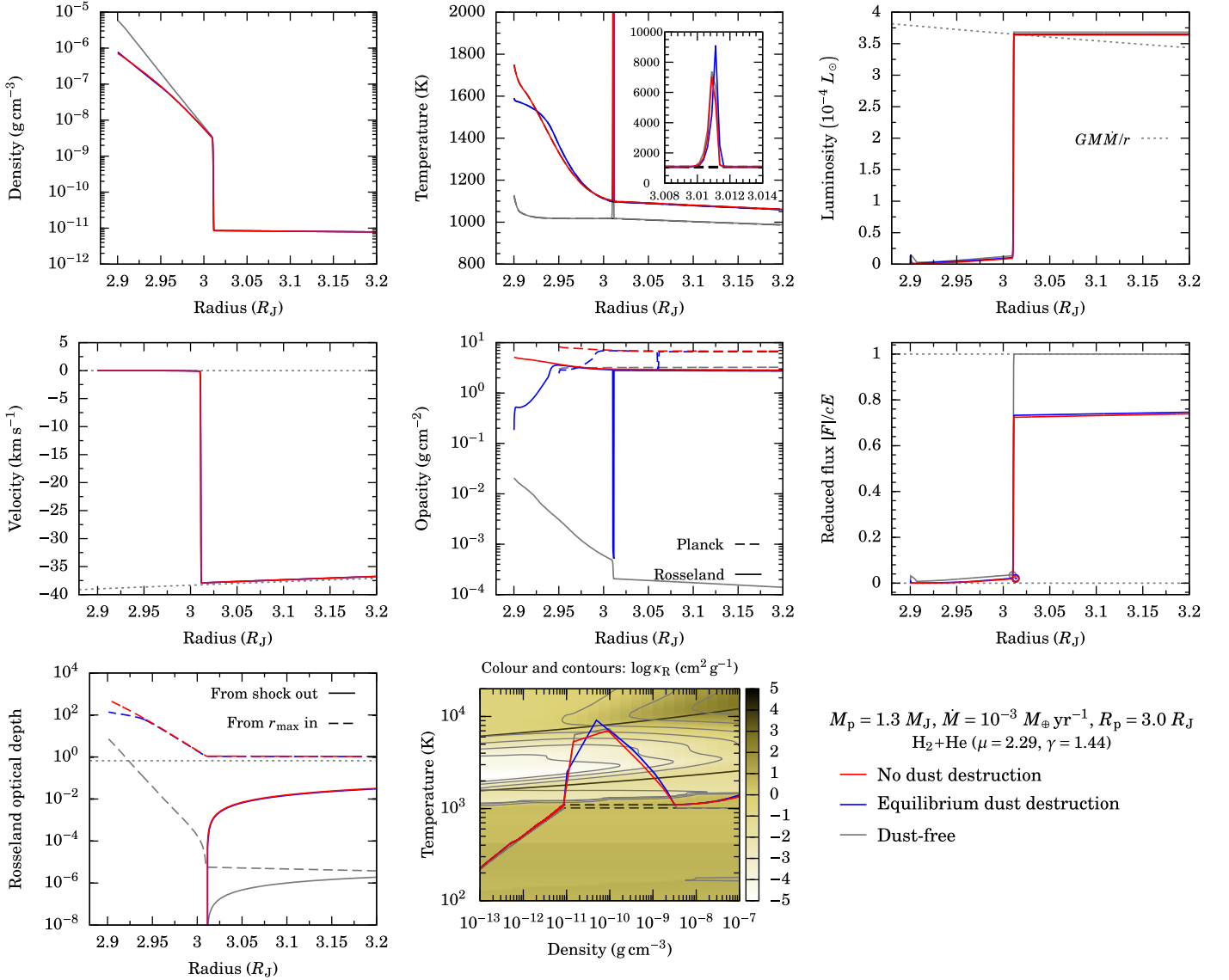
Figure 10. Structure of the shock for different behaviors of the dust in the Zel'dovich spike: no destruction (*red curves*) or equilibrium destruction (nominal case; *blue curves*). For comparison, a case with no dust opacity at all is also shown (*gray*). In the top and bottom middle panels, the radiation temperature is shown as dashed black lines. In the opacity panel, the Planck curves are shifted by 0.05 R_J to the right for clarity. Note that the Planck opacity is high ($\kappa_P \gtrsim 3$ cm^2 g^{-1}) even in the absence of dust and that the gas and radiation are tightly coupled, with $T_{rad} \neq T_{gas}$ only in the Zel'dovich spike (see the middle panels in the top and bottom rows). The solid black lines in the bottom middle panel display for reference where hydrogen is dissociated or ionized to 50% (SCvH), and the gray contours are for integer values of $\log \kappa_R$ ($cm^2\ g^{-1}$).

Equation (45) is an upper bound in the case $\gamma < 4/3$ because any flattening of the luminosity profile as in Figure 9 will slow down the decrease of $T(r)$. For $\gamma > 4/3$ the estimate is more like a lower bound, but because the critical $\gamma = 4/3 \approx 1.33$ is not far from $\gamma = 1.44$ for molecular hydrogen with helium, it is also roughly equal to the actual change in that case. This can be seen graphically in Figure 9.

Thus, in Figure 9, $L(r)$ increases outward for the high-γ cases ($\gamma = 5/3$) as well as for the nominal case ($\gamma = 1.44$), while it slightly decreases overall for the low-γ cases ($\gamma = 1.1$). The mean molecular weight also plays a role, and, in all, L at roughly the Hill radius varies by roughly 10% for this specific ($\dot{M}$, M_p, R_p) case over all (γ, μ) combinations. In Section 7.3 we look at this more generally.

However, the size of the luminosity jump ΔL at the shock is very nearly the same across all simulations in Figure 9. Because in all cases the immediate upstream region is in the

free-streaming regime, the small differences in $L(r_{shock}^{+})$ are related to the slightly different downstream luminosities or, equivalently, $f_{red}(r_{shock}^{-})$.

6.1.3. Global Physical Efficiency

Finally, depending on both γ and μ, the global physical efficiency ranges from $\eta^{phys} = 84\%$ to 98%, increasing with μ but decreasing with γ. This large difference comes from different γ values but also from the changing Mach number (through μ), as can be seen from Equation (38). One can wonder whether a low μ caused by ionization could lead to much lower Mach numbers and thus efficiencies. However, because the Mach numbers we find are all high ($10 \lesssim \mathcal{M} \propto 1/\sqrt{\mu}$), even a change by a factor of at the very most $\sqrt{0.6/2.3} = 0.5$ (from ionized to molecular gas) would leave $\mathcal{M} \gtrsim 5 > 2.5$ and thus the shock supercritical for a given T_{shock} and v_{ff}. This statement should still
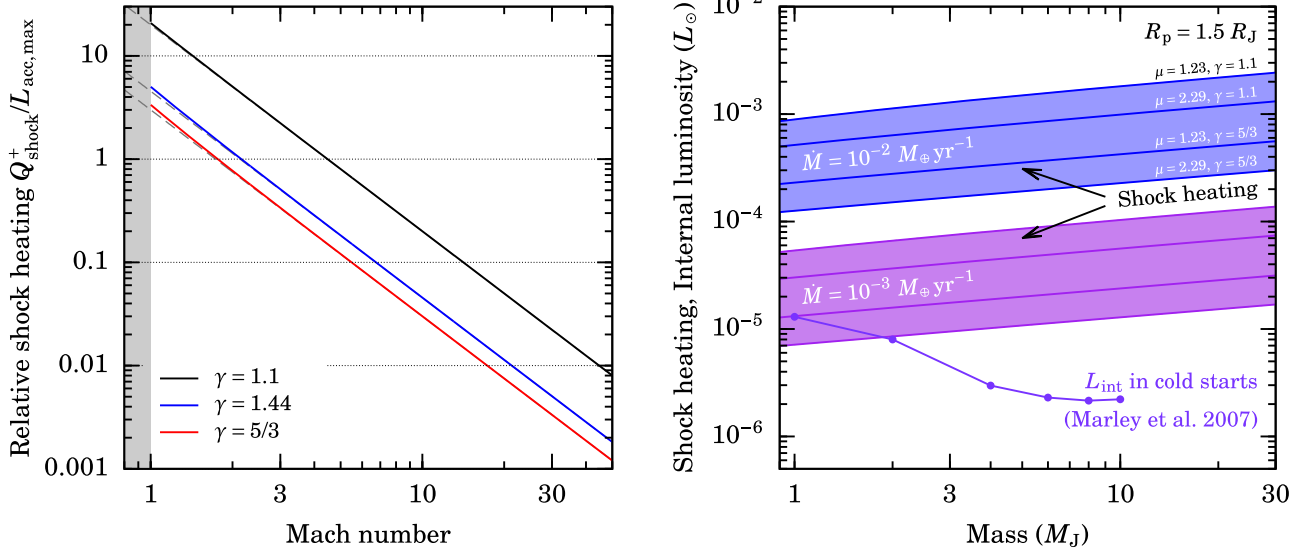
Figure 11. Estimated heating of the planet by the shock. Left panel: heating Q_{shock}^+ relative to the maximum accretion luminosity $L_{acc,max} = GM_p\dot{M}/R_p$ for an isothermal shock (Equation (49)) as a function of the preshock Mach number for different γ. Below $\mathcal{M} = 1$ there is no shock (grayed-out region). The large-$\mathcal{M}$ limit $Q_{shock}^+/L_{acc} = 2/[(\gamma - 1)\mathcal{M}^2]$ is also shown (dashed gray lines). Right panel: absolute Q_{shock}^+ (Equation 50(c)) for $\dot{M} = 10^{-2}$ (blue shaded region) and $10^{-3} M_\oplus$ yr^{-1} (purple). We neglect L_{dnstr} in Q_{shock}^+ and take $R_p = 1.5 R_J$ for all masses. We also show the approximate internal luminosity L_{int} from the Marley et al. (2007) cold starts during formation, which accrete mostly at $\dot{M} \approx 10^{-2} M_\oplus$ yr^{-1}. The shock heating clearly dominates L_{int}.

be revisited with simulations using the full EOS because $\mathcal{M}$ is of course a function of T_{shock}.

6.1.4. Other Quantities

The other panels of Figure 9 are shown for completeness. The profiles are qualitatively similar between all simulations (see the detailed description in Paper I), and we can mention here that we find that the gas and radiation are always well coupled, which is presumably related to the sufficiently high opacity. Moreover, as in Paper I, the radiative precursor to the shock is larger than the simulation box, as even a cursory comparison to standard supercritical and subcritical shock structures (e.g., Ensman 1994) reveals.

6.1.5. Summary of the Effect of the EOS

In summary, depending on the EOS, a different luminosity reaches the accretion radius, but the variation is moderate (tens of percent) across the relevant input parameter range. However, both the shock temperature and the ram (postshock) pressure are independent of the perfect EOS, at least in the limit of an isothermal shock. This is an important result. We conjecture that the postshock temperature and pressure will not be different when an ideal but nonperfect EOS is used instead. This will need to be verified, but if if holds, and if the shock is still isothermal, it implies that the postshock entropy s_{post}, which depends only on T and P, will be the same as found here. As for the shock efficiency, it clearly depends on the EOS (see Figure 9).

6.2. Influence of the Dust Opacity

Simulations such as those presented here do not spatially resolve the physical Zel'dovich spike (see Appendix B of Vaytet et al. 2013b), which is typically much thicker than the mean free path of the gas particles but still orders of magnitude smaller than a photon mean free path (Zel'dovich & Raizer 1967; Drake 2007). The peak temperatures should be

very high but the cooling behind the peak also very quick, so that the fate of dust grains passing through this shock is not obvious a priori. Calculating their time-dependent sublimation and recondensation including nonequilibrium effects is beyond the scope of this work. Because our standard assumption is to use time-independent (equilibrium) abundances from the simple model of Isella & Natta (2005), in which the destruction temperature is simply $T_{dest} = 1220 \times \rho_{-11}^{0.0195}$ K, where $\rho_{-11} \equiv \rho \times 10^{11}$ cm^3 g^{-1}, we consider in this section the other extreme, namely that the grains are not destroyed. Note that the question of the dust (non-)destruction in the shock poses itself only for shocks at low enough temperature that solid grains are still present the incoming material (e.g., the $\approx 1 M_J$ cases at $\dot{M} = 10^{-3} M_\oplus$ yr^{-1} in Figure 3).

Figure 10 shows the resulting shock structure for constant dust abundance in red and equilibrium abundances in blue. In all relevant quantities (ρ, v, T, L, f_{red}), with the obvious exception of κ_R and κ_P, the profiles are essentially identical for these two cases. This also holds throughout the simulation domain (not shown). In particular, the shock temperature is the same, and the Zel'dovich spike stays very optically thin (as it should), increasing from, very roughly, $\Delta\tau_R \sim 10^{-5}$ to 10^{-2}. Note that the opacity is too high in the always-dust case (see blue solid line in opacity panel), but this does not affect the temperature structure of higher postshock regions, i.e., directly below the shock.

As a more extreme case, we also switched off the dust contribution entirely, shown by gray profiles in Figure 10. This represents the limiting case of the reduction of Szulágyi et al. (2017) by a factor of 10 relative to the interstellar medium, on the grounds that the growth of dust grains into larger aggregates diminishes the opacity. As pointed out by Uyama et al. (2017), dust also tends to settle to the midplane while accretion comes from higher up in the circumstellar disk, so that the accretion flow onto a planet is actually possibly devoid of dust.

Leaving out the dust opacity lowered the Rosseland mean by four orders of magnitude near the shock but the Planck mean only by a factor of two due to the high Planck opacity of the gas. The consequence was a decrease in shock temperature by only 100 K, associated with a jump in the reduced flux increasing from $\Delta f_{\mathrm{red}} \approx 0.7$ to $\Delta f_{\mathrm{red}} \approx 1$.

Our conclusion from this test is that the upstream f_{red} (given $f_{\mathrm{red}} \approx 0$ downstream), and hence ultimately the opacity there, is important in setting the shock temperature, but that the dust destruction in the Zel'dovich spike is not. This seems to imply that one would need to follow the time-dependent evaporation of the dust *approaching the shock* in each simulation because the outer parts are always cold enough for dust to be present.[12] However, this will affect only a very small fraction of cases. Indeed, it requires (i) preshock temperatures above the (density-dependent) dust destruction temperature but (ii) not too high to not already have the dust destroyed at a large distance ahead from shock, in which case the dust would certainly be evaporated. The transition region is very narrow in temperature ($\Delta T \sim 100$ K; Semenov et al. 2003) compared to the range of shock temperatures we can expect (see, e.g., Figure 3). For these cases where it is relevant, a zeroth-order approach would be to compare the flow timescale $t_{\mathrm{flow}} = r/v$ to the evaporation time as given by the Polanyi-Wagner formula (see, e.g., Equation (20) of Grassi et al. 2017). However, this is an only marginally important consideration and will not be investigated further.

7. Discussion

We discuss some of the results presented here.

7.1. Hot Starts or Cold Starts?

The main question driving this work is whether the processing of the accreting gas through the shock leads to hot starts or cold starts (Marley et al. 2007). While a detailed coupling of the shock results to formation calculations is needed to resolve this, there are several ways of estimating the outcome beforehand. We now consider them in turn.

7.1.1. Luminosity-based Argument: Shock Heating versus Internal Luminosity

The classical understanding of the extreme outcomes considers that the accreting gas carries only kinetic energy and that for cold starts, *all* of this incoming energy is radiated away at the shock, with no energy brought into the planet, while for hot starts, none of the incoming energy should leave the system but instead is added to the planet. However, this view neglects the thermal energy of the gas that is brought into the planet, which comes from preheating by the radiation from the shock. In Paper I we have shown that this is in fact not negligible, leading to the definition of η^{phys} instead of η^{kin} (see Section 4.4). Therefore, it is possible for most of the accretion energy to be radiated away at the shock, but to still have an important heating of the planet by the shock if the inward heating is high compared to the internal luminosity.

To quantify this, at least when following the global energetics alone, one can look at the effective heating by the

shock Q_{shock}^{+} (to be defined shortly) relative to the internal luminosity L_{int},

$$q_{\mathrm{shock,rel}}^{+} \equiv \frac{Q_{\mathrm{shock}}^{+}}{L_{\mathrm{int}}}. \tag{47}$$

A high $q_{\mathrm{shock,rel}}^{+}$ would suggest that the shock can heat up the planet appreciably.

The effective heating of the planet by the shock, in turn, is the net rate of total energy that is not lost from the system and therefore added to the planet. By the definition of η^{phys} (Equation (10)), this is

$$Q_{\mathrm{shock}}^{+} = (1 - \eta^{\mathrm{phys}})|\dot{E}(r_{\mathrm{max}})| = |\dot{E}(r_{\mathrm{shock}}^{-})|, \tag{48}$$

where r_{shock}^{-} is immediately downstream of the shock. From the definition of $\dot{E}$ (Equation (11)), we have in the isothermal limit that is applicable to our results

$$Q_{\mathrm{shock}}^{+} = \dot{M}[h(r_{\mathrm{shock}}^{-}) + e_{\mathrm{kin}}(r_{\mathrm{shock}}^{-})] \tag{49a}$$

$$= \left(1 + \frac{\gamma - 1}{2\gamma^2 \mathscr{M}^2}\right)\dot{M}h(T_{\mathrm{shock}}) \tag{49b}$$

$$= \left(1 + \frac{\gamma - 1}{2\gamma^2 \mathscr{M}^2}\right)\frac{\gamma}{\gamma - 1}\frac{k_{\mathrm{B}}T_{\mathrm{shock}}}{\mu m_{\mathrm{H}}}\dot{M} \tag{49c}$$

$$= \left(\frac{2}{(\gamma - 1)\mathscr{M}^2} + \frac{1}{\gamma^2 \mathscr{M}^4}\right)L_{\mathrm{acc,max}}, \tag{49d}$$

using also that for an isothermal shock the post- and preshock densities are related by $\rho_2 = \rho_1 \gamma \mathscr{M}^2$ and that $\rho_2 v_2 = \rho_1 v_1$. We recall that $L_{\mathrm{acc,max}} = GM_{\mathrm{p}}\dot{M}/R_{\mathrm{p}}$. Equation 49(b) in particular shows that what is added to the planet is mostly the enthalpy of the gas, with a small additional term corresponding to the leftover kinetic energy (from the postshock settling velocity of the gas). The latter is vanishingly small in the limit of a high preshock Mach number.

The shock heating relative to $L_{\mathrm{acc,max}}$ is plotted against Mach number in Figure 11(a). It may seem surprising that for low Mach numbers $\mathscr{M} < 2$–4 (depending on γ), we have that $Q_{\mathrm{shock}}^{+} > L_{\mathrm{acc,max}}$. However, this simply comes from the fact that the gas at r_{max} does not bring only kinetic energy but also enthalpy with it.

For the range $\mathscr{M} \approx 7$–35 (looking at Figures 4 and 8) and with $\gamma = 1.44$ as we used here, we see from Figure 11(a) that $Q_{\mathrm{shock}}^{+} \approx (10\%\text{–}0.4\%)L_{\mathrm{acc}}$, respectively. In this high-Mach number limit (valid actually already for $\mathscr{M} \gtrsim 1$), the effective heating rate can be simplified to

$$Q_{\mathrm{shock}}^{+} = \frac{2}{\gamma - 1}\frac{L_{\mathrm{acc}}}{\mathscr{M}^2} \tag{50a}$$

$$= \frac{\gamma}{\gamma - 1}\frac{k_{\mathrm{B}}}{\mu m_{\mathrm{H}}}\left(\frac{GM_{\mathrm{p}}\dot{M}^5}{16\pi\sigma R_{\mathrm{p}}^3}\right)^{1/4}\ell^{1/4} \tag{50b}$$

---

[12] It is easy to estimate, assuming $T \propto r^{-1/2}$, that only unrealistic parameter combinations could lead to evaporated dust (i.e., $T \gtrsim 1000$ K, taking the density dependence into account) at $r \sim k_{\mathrm{Lissauer}}R_{\mathrm{Hill}}$ or $r \sim R_{\mathrm{Bondi}}$.

$$= 3 \times 10^{-4} L_\odot \frac{\gamma_{1.44}}{\gamma_{1.44} - 1} \left(\frac{\mu}{2.29} \right)^{-1} \ell^{1/4}$$

$$\times \left(\frac{\dot{M}}{10^{-2} \, M_\oplus \, \mathrm{yr}^{-1}} \right)^{5/4} \left(\frac{R_\mathrm{p}}{1.5 \, R_\mathrm{J}} \right)^{-3/4}$$

$$\times \left(\frac{M_\mathrm{p}}{10 \, M_\mathrm{J}} \right)^{1/4}, \tag{50c}$$

where again $\ell = 1 + L_\mathrm{dnstr}/L_\mathrm{acc,max}$, the downstream luminosity $L_\mathrm{dnstr} = L_\mathrm{int} + L_\mathrm{compr}$ being the sum of the luminosity coming from the deep interior and the compression luminosity, and writing $\gamma_{1.44} \equiv \gamma/1.44$. For Equations 50(b) and (c), we took the free-streaming limit for the shock temperature (Equation (33)), which was seen to hold over most of parameter space. As in Equation (33), ℓ formally depends on $(\dot{M}, M_\mathrm{p}, R_\mathrm{p})$, but this dependence is negligible in the limit of $L_\mathrm{dnstr} \ll L_\mathrm{acc,max}$.

Mordasini et al. (2017) have demonstrated that not only a "hot accretion", but even a "cold nominal" formation scenario leads to warm starts. Therefore, we estimate $q^+_\mathrm{shock,rel}$ with the cold starts of Marley et al. (2007), which represent a conservative lower limit to the entropies and luminosities of planets during their formation. Because Marley et al. (2007) do not report the internal luminosities of their planets during formation, we need to estimate them. Their Figure 4 shows that right after formation, the cold starts stay within 90% of the initial luminosity for a timescale $t_{90} \lesssim 1 \, \mathrm{Myr}$ for $1 \, M_\mathrm{J}$, 1–2 Myr for $2 \, M_\mathrm{J}$, and ~6 Myr and increasing for $4 \, M_\mathrm{J}$ and up.[13] The time spent in runaway accretion in their models is around $t_\mathrm{acc} = 0.1$ Myr to 0.5 Myr for 1 to $10 \, M_\mathrm{J}$, respectively. Thus even for $M_\mathrm{p} = 1 \, M_\mathrm{J}$, the cooling timescale t_{90} is much longer than t_acc, and it should be a reasonable approximation to assume that the internal luminosity and the radius do not change considerably between the last stages of the runaway accretion phase—when, for example, more than half the planet mass has been assembled—and right after.

Figure 11(b) displays the approximate heating by the shock (Equation 50(c)). Considering the extreme combinations of μ and γ as in Section 6, we find $Q^+_\mathrm{shock} \approx 10^{-4}$–$10^{-3} \, L_\odot$ for $\dot{M} \approx 10^{-2} \, M_\oplus \, \mathrm{yr}^{-1}$ and $Q^+_\mathrm{shock} \approx 10^{-5}$–$10^{-4} \, L_\odot$ for $10^{-3} \, M_\oplus \, \mathrm{yr}^{-1}$. The radius is fixed at $R_\mathrm{p} = 1.5 \, R_\mathrm{J}$, a typical value for forming planets (Mordasini et al. 2012a), but varying it in a reasonable range $R_\mathrm{p} \approx 1$–$3 \, R_\mathrm{J}$ does not change the outcome qualitatively.

We compare in Figure 11(b) the shock heating to the internal luminosity of the Marley et al. (2007) cold starts. In their model, most of the mass is accreted with $\dot{M} \approx 10^{-2} \, M_\oplus \, \mathrm{yr}^{-1}$ with a linear decrease of $\dot{M}$ toward the end (Hubickyj et al. 2005; Marley et al. 2007). Thus, the relevant heating is around $Q^+_\mathrm{shock} > 10^{-4} \, L_\odot$. This is one to two orders of magnitude higher (!) than the (post-)formation luminosities

---

[13] Alternatively, one could look at the e-folding times of the luminosity, which are 4 Myr for $t_\mathrm{exp} = 1 \, M_\mathrm{J}$, 10 Myr for $2 \, M_\mathrm{J}$, 60 Myr for $4 \, M_\mathrm{J}$, and increasing. Note that the Kelvin–Helmholtz times $t_\mathrm{KH} = GM_\mathrm{p}^2/R_\mathrm{p}L_\mathrm{p} = 1 \, \mathrm{Gyr} \, (M_\mathrm{p}/4 \, M_\mathrm{J})^2/[(R_\mathrm{p}/1.3 \, R_\mathrm{J})(L_\mathrm{p}/3 \times 10^{-6} \, L_\odot)]$ are longer than these e-folding times by roughly a large factor of 30 (i.e., ca. 1.5 dex). Note that t_KH is within ca. ± 0.5 dex of the cooling time $t_S = M_\mathrm{p} \overline{T} S/L_\mathrm{p}$ defined in Marleau & Cumming (2014), where S is the entropy of the planet and $\overline{T}$ the mass-weighted average temperature of the planet is within approximately ± 0.5 dex. Thus both t_S and t_KH are hardly adequate proxies for t_{90} or t_exp, and one must exercise caution when using t_KH in timescale-based arguments.

$L_\mathrm{int} \approx 10^{-6} \, L_\odot$ of Marley et al. (2007). At $1 \, M_\mathrm{J}$, the heating could be only moderate, but for $M_\mathrm{p} \gtrsim 2 \, M_\mathrm{J}$, the conclusion becomes more secure. Moreover, taking $L_\mathrm{dnstr} \neq 0$ into account for the estimate would only lead to a lower Mach number and thus a higher Q^+_shock.

Thus, based on this a posteriori comparison of the internal luminosity and of the energy input rate, the shock is expected to heat up planets in the "cold classical" approach (Marley et al. 2007; Mordasini et al. 2017). The importance of the shock should increase with planet mass.

7.1.2. Shock-temperature-based Argument

Berardo & Cumming (2017) and Cumming et al. (2018) followed the time-dependent internal structure of accreting planets with constant accretion rates. They specified their outer boundary conditions for the planet structure as a temperature T_0 at a pressure equal to the ram pressure, $P_0 = P_\mathrm{ram}$. Berardo & Cumming (2017) report that setting T_0 as a fraction[14] f of the free-streaming temperature $T_\mathrm{sh,fs}$ (plus a relative contribution from the internal luminosity) led to fully radiative interiors at the end of formation for f above a certain f_min. Lower values of f resulted in convective interiors. The minimum fraction f_min was lower for higher accretion rates, with $f_\mathrm{min} \approx 1$ for $\dot{M} = 10^{-3}$ and $f_\mathrm{min} \approx 0.1^{1/4} \approx 0.6$ for $\dot{M} = 10^{-2} \, M_\oplus \, \mathrm{yr}^{-1}$. Because we find $f \geqslant 1$—i.e., the temperature at the ram pressure matches the temperature in the $\eta^\mathrm{kin} = 100\%$ limit (Equation (33))—we expect formation calculations using our results to lead to radiative planets. Note that even though we considered only $L_\mathrm{int} = 0$ here, we expect the same result ($\eta^\mathrm{kin} = 1$ and thus $f = 1$) to hold for nonzero interior luminosity. It should still be explored systematically, however, especially because the result of Berardo & Cumming (2017) was for a specific choice of pre-runaway entropy of the planet S_i, and it is the contrast between this entropy S_i and the immediate postshock entropy $S_0 = S(T_0, P_0)$ that matters (Berardo et al. 2017).

7.1.3. Entropy-based Argument

Because our postshock entropies are higher or much higher than postformation entropies (and thus, neglecting cooling, entropies during formation) of Mordasini et al. (2017), we certainly do not expect the shock to be able to cool the planet as it accretes. Berardo et al. (2017) found that they needed extremely low shock entropies (with temperatures of about $T_\mathrm{shock} \approx 150 \, \mathrm{K}$) to reproduce the cold starts of Marley et al. (2007). We find $T_\mathrm{shock} > 1000 \, \mathrm{K}$, however, down to $\dot{M} = 10^{-3} \, M_\oplus \, \mathrm{yr}^{-1}$. Thus the high postshock entropy will at least slow down the cooling of the planet during its formation (the "stalling" regime of Berardo et al. 2017), if not heat the planet ("heating regime"), but should not allow for any decrease of the entropy ("cooling regime"). From this argument too, then, cold starts seem unlikely.

---

[14] These authors write $T_0^4 = \chi T_\mathrm{acc}^4 + T_\mathrm{eff}^4$, but their T_acc differs from our equivalent quantity, $T_\mathrm{sh,fs}$, with $T_\mathrm{acc} = 4^{1/4} T_\mathrm{sh,fs} \approx 1.4 T_\mathrm{sh,fs}$ in the case of $\ell = 0$ in Equation (33). We therefore here use f and not χ. Note also that χ in Cumming et al. (2018) was written as η in Berardo & Cumming (2017), but that it should not be confused with the efficiency. Our f here can be larger than 1, which occurs when the preshock $\kappa_\mathrm{R} \rho R_\mathrm{p}$ is large (see Section 5.3).

7.2. Opacities and Gas–radiation Coupling

Next we discuss the opacities. We have seen in detail in this work that the Rosseland mean controls the extent to which radiation is diffusing as opposed to freely streaming. As for the Planck opacity, it is an important factor in determining the extent to which the opacity carrier (gas or dust) and the radiation are in equilibrium. Indeed, the inflowing matter will equilibrate with the outgoing radiation, leading to $T_{gas} \approx T_{rad}$, if the energy exchange time (controlled by the absorption coefficient $\rho\kappa_P$; see Malygin et al. 2017) is shorter than the time needed for the gas to reach the shock (controlled by v_{ff}). Therefore we take a critical look at uncertainties concerning the opacities.

1. We find that everywhere except in the shock (in the Zel'dovich spike), the preshock temperatures of the gas and radiation are equal. Simulations that use none-quilibrium radiation transport with tables with unrealistically low Planck mean values (see Figure 2(b)) might not find that the shock is able to preheat the gas. Thus it is an important result that the Planck values are high enough for the radiation and gas to be coupled.

2. A quite uncertain aspect of dust opacity computations is the distribution of dust grain properties (size, porosity, composition, etc.) and also their sublimation. However, we found that the exact opacity in the accretion flow does not matter for the shock temperature. This effectively removes a source of uncertainty and makes the derived shock temperatures more robust.

3. Nevertheless, the presence of dust in the accretion flow was seen to affect the temperature at and beyond the dust destruction front (see Stahler et al. 1980; Vaytet et al. 2013a) and thus also the luminosity at the Hill sphere. With a dust destruction front, the temperature there and beyond remains higher by up to a factor of several compared to the expression for a constant-(L/f_{red}) profile, Equation (43) (although with the same power-law dependence). The decrease or increase in *luminosity* between the shock and the Hill sphere is also different from the case without a dust destruction front (see Section 6.1). However, if the dust in the incoming flow is strongly depleted relative to the interstellar medium abundance assumed in Semenov et al. (2003), the flow will tend more to be in the free-streaming regime, and its temperature is thus given by Equation (43).

4. We conducted tests as in Paper I with constant low opacity. Typically, as we verified separately (not shown), at lower values $\kappa_R = \kappa_P \sim 0.01$ cm^2 g^{-1}, the radiation and gas temperatures stay decoupled even in the high-density postshock region. This is entirely unrealistic, however, given that at these densities ($\rho \approx 10^{-10}$–10^{-8} g cm^{-3}) and temperatures ($T_{gas} \approx 500$–5000 K; see Figure 4 of Paper I) the Planck opacity is rather of order $\kappa_P \sim 10$ cm^2 g^{-1} (Figure 2(b)).

5. Finally, we related the behavior of the opacity to that of the temperature and thus also of the luminosity (Section 5.1). This makes it now possible to understand the "bursts" in L seen, e.g., at 0.3 au in Figure 8 of Vaytet et al. (2013a), who also use FLD, but kept the frequency dependency. These bursts are associated with sharp opacity transitions in the respective wavelength band (in particular at the dust destruction front) and with slight changes of slope in the temperature.

We note that it is in the Zel'dovich spike that nonequilibrium (2-*T*) effects lead to the formation of observable spectral tracers of accretion onto protostars and brown dwarfs (Hartmann et al. 2016; Santamaría-Miranda et al. 2018). This emission is discussed for the shock onto the circumplanetary disk in Aoyama et al. (2018) and for the accretion shock on the planet surface in a forthcoming publication (Y. Aoyama et al. 2019, in preparation).

7.3. Equation of State

In these first two papers (Paper I, this work) we have restricted ourselves to a perfect EOS (constant μ and γ). To first order, this should not affect our main results. However, (i) the luminosity in the accretion flow (and thus at the Hill sphere), (ii) the postshock compression luminosity, and thus also (iii) the more precise value of T_{shock} (through the Δf_{red} factor) should all be affected to some extent by the EOS, at least for some combinations of ($\dot{M}$, M_p, R_p).

Concerning item (i), we studied in Section 6.1.2 an estimate $\Delta L_{(43)}$ of the drop or increase in the luminosity between the shock and the Hill radius. In the limit of a perfect EOS and of temperature profile $T \propto r^{-1/2}$, Equation (45) shows that the ratio $|\Delta L_{(43)}|/L_{acc}$ is highest for high accretion rates, low masses, and high radii. Over $\dot{M} = 10^{-3}$–10^{-2} $M_\oplus$ yr^{-1}, $M_p = 1$–10 M_J, and $R_p = 1$–5 R_J (an even wider parameter space than what we consider for our simulations), the relative drop or increase is never larger than $|\Delta L_{(43)}|/L_{acc} \approx 10\%$–15%, taking the extreme case of ($\mu = 1.23$, $\gamma = 1.1$). Taking the actual temperature profile into account (as opposed to assuming $T \propto r^{-1/2}$ everywhere) will change this somewhat, but usually only to make it smaller. In any case, the variation in L across the Hill sphere is unimportant compared to the effect of other simplifications of our model. We note that for molecular hydrogen and neutral helium (our default case), the actual change in L (i.e., as measured from the simulation and not using a simple $T \propto r^{-1/2}$ profile) is less than 2% for any ($\dot{M}$, M_p, R_p) considered here.

We report already here that preliminary estimates suggest that for simulations with a full EOS, the change in luminosity across the Hill radius is at most approximately 20%, which is thus noticeable but also not large. Details will be presented in a forthcoming publication.

Finally, the relative smallness of the luminosity change $\Delta L_{(43)}$ justifies a posteriori the assumption of constant (L/f_{red}) made to derive it. Indeed, a relative change $|\Delta L_{(43)}|/L_{acc} \approx 10\%$–15% over 2–3 dex in radius (from $R_p \approx 1$–3 R_J to $R_{acc} \approx k_{Lissauer}R_{Hill}(M_p) \approx 250$–$500$ R_J for $M_p \approx 1$–10 M_J at 5.2 au) corresponds to an approximate average slope (see Equation (30)) of at most $|\beta| \approx \log_{10}(1.15)/2 = 0.04$ if f_{red} is constant or $|\beta| \approx 0.4$ at most if f_{red} also changes by a factor of approximately 3, as in Figure 9. Thus even for these conservative estimates, we find $|\beta| \ll 2$, justifying a posteriori the assumption of a constant L/f_{red} used to derive the change in L.

8. Summary and Conclusions

In this series of papers (Paper I; this work; G.-D. Marleau et al. 2019, in preparation) we take a detailed look at the physics of the accretion shock in planet formation. In this second paper, we have updated to disequilibrium (2-*T*) radiation transport (i.e., following the gas and radiation energy

densities separately) and modern opacities, especially for the gas: we use the dust opacities of Semenov et al. (2003) but the gas opacities of Malygin et al. (2014), avoiding the too-low Planck mean opacities that are normally included in Semenov et al. (2003). We have now also surveyed a range of values for the formation parameters ($\dot{M}$, M_p, R_p), assuming negligible L_int (see Figure 1), namely $\dot{M} = 10^{-3}$–$10^{-2}\,M_\oplus\,\text{yr}^{-1}$, $M_\text{p} \approx$ 1–10 M_J, $R_\text{p} \approx 1.6$–3 R_J. This has motivated us to several semianalytical derivations along with comparisons to simulation outputs. We have kept the simplification of a perfect EOS and focused on the case of molecular hydrogen with a cosmic admixture of helium ($\mu = 2.29$, $\gamma = 1.44$).

We now summarize our primary findings on different aspects. Concerning the thermal and radiative properties of the accretion flow:

1. Both our simulations and analytical theory show that the behavior of the luminosity in the accretion flow is not the direct result of radiative transfer effects but rather depends on the EOS (Section 6.1.2). The luminosity turns out to be radially constant to ≈ 2 % for values of μ and γ appropriate for $H_2 + He$. Taking other values of μ and γ increases or decreases the change in L between the shock and roughly the Hill sphere. However, the maximum change is relatively small with $|\Delta L_{(43)}|/L_\text{acc} \lesssim 15$ % across the relevant parameter space and for any ($\gamma \geqslant 1.1$, $\mu \geqslant 1.23$) combination (Section 7.3). We highlight that the $\Delta\tau_\text{R} \sim 1$ surface is not of any particular significance (Section 4.3).

2. Thanks to the sufficiently high Planck mean opacities (for which a contribution from the dust is not needed), the matter and radiation are very well coupled both ahead of and behind the shock, i.e., everywhere except in the Zel'dovich spike (Figures 2 and 9). In fact, nonequilibrium (2-T) radiation transport could be neglected when studying only the postshock temperature and pressure or the global energetics.

3. As found in Paper I and confirmed here, the radiative precursor to the shock (Mihalas & Mihalas 1984; Commerçon et al. 2011a) is larger than the simulation domain, which is roughly the Hill sphere, even in the case of somewhat high Rosseland optical depth ($\Delta\tau_\text{R} \sim 10$).

4. The preshock region close to the planet, out to some Rosseland optical depth, is usually in the free-streaming regime and not, as one would expect for a supercritical shock, in the diffusion limit (e.g., Figure 8 of Vaytet et al. 2013b). Thus the shock is a thick–thin shock in the classification of Drake (2006). At low shock temperatures ($T \lesssim 1500\,\text{K}$) the dust is still present, making the preshock region somewhat diffusive and raising the shock temperature.

The shock properties were a focus of this study, and we found the following:

1. As in Paper I, all shocks are isothermal and supercritical, and the Mach numbers are high enough for $\eta^\text{kin} \approx 100\%$ of the incoming kinetic energy flux to be converted to radiation *locally at the shock* (see gray lines in Figures 4 and 8). The postshock pressure is equal to the ram pressure P_ram.

2. The free-streaming analytical estimates of the shock temperature (Equation 6(b)) and of the upstream luminosity (Equation (8)) were seen to hold very well

over a large portion of parameter space. Importantly, we found out that this holds also for high optical depths between the shock and the nebula. Deviations of $\sim 5\%$ in T occur at low shock temperatures (Figure 3(a)).

3. An important analytical development was the derivation of an implicit (Equation (35)) for the shock temperature T_shock given a Rosseland mean opacity function $\kappa_\text{R}(\rho, T_\text{shock})$. We solved this numerically (Figure 7).

4. Based on our analysis, T_shock should not be affected to first order by the use of an nonperfect ideal EOS (i.e., considering dissociation and ionization) because γ and μ do not enter in the derivation of T_shock (see Equation (32)). However, (i) the luminosity in the accretion flow (and thus at the Hill sphere), (ii) the postshock compression luminosity, and thus also (iii) the more precise value of T_shock (through the Δf_red factor; Equation (6)) should all depend somewhat on the EOS. This will be assessed in a subsequent paper (G.-D. Marleau et al. 2019, in preparation).

5. We calculated the postshock entropies immediately below the shock using an EOS taking dissociation into account (Appendix A of Berardo et al. 2017). While this is formally not consistent with our (perfect-EOS) simulations, we argued that this is likely accurate because T_shock and $P_\text{post} = P_\text{ram}$ are probably independent of the EOS. The immediate postshock entropies were found to be between approximately 13 and 20 $k_\text{B}\,m_\text{H}^{-1}$ for our range of parameters (Section 4.6, Figure 5). These values are high compared to the postformation entropy of planets, which is at most around 10–14 $k_\text{B}\,m_\text{H}^{-1}$ according to current, though not definitive, predictions (Mordasini 2013; Berardo & Cumming 2017; Berardo et al. 2017; Mordasini et al. 2017). However, we caution and emphasize that the actual entropy of the gas added to the planet, below the postshock settling layer, is different from this immediate postshock entropy. This is explored in Berardo et al. (2017) and Berardo & Cumming (2017).

Finally, a key output of our simulations was the efficiency of the shock:

1. We have measured the physical efficiency η^phys as a function of accretion rate $\dot{M}$, planet mass M_p, and planet radius R_p (Figure 5) and derived it semianalytically (Equations (13) and (38)). This efficiency captures the global energy recycling that occurs in the preshock region (Paper I). We saw (Figure 5) that the efficiencies are always greater than roughly 97% for the range of parameters considered here.

2. Naively, a high η^phys could suggest that the gas is added "cold", but the part that does not escape (i.e., the heating of the planet by the shock) turns out to be much larger than the internal luminosity in the Marley et al. (2007) extreme cold starts (Section 7.1.1).

The semianalytical work presented here revealed the reduced flux $f_\text{red} = F_\text{rad}/(cE_\text{rad})$ (Equation (7)) to be a powerful quantity for understanding the behavior of the radiation field (free streaming or diffusing, often termed approximately "optically thin" and "optically thick"). This holds at least for the gray treatment of radiation transport used in this work in a spherically symmetric geometry. When L/f_red is sufficiently constant radially, we showed in Equation (31) that there is a simple relation between the reduced flux f_red and the opacity, which provides an intuitive understanding of f_red.

The main results of our simulations are postshock (P, T) values and global efficiencies η^{phys}. This is useful for detailed modeling of the structure of accreting planets as in Berardo et al. (2017), Berardo & Cumming (2017), and Cumming et al. (2018), and also for the one-zone global approach of, e.g., Hartmann et al. (1997). The Bern model (Alibert et al. 2005; Mordasini et al. 2012b, 2017) is currently in between, calculating detailed planet structures but with the assumption of a radially constant luminosity. Note that the modeling of the energy transfer at the accretion shock is also relevant in the context of star formation (e.g., Baraffe et al. 2012; Geroux et al. 2016; Baraffe et al. 2017; Jensen & Haugbølle 2018). Researchers interested in using our simulation results can take the semianalytical formulæ presented above, including the opacity effects for the temperature, under the assumption of a perfect EOS.

The other main outcome is the amount of radiation that reaches the Hill sphere. This should be useful input for studies of the thermo-chemical feedback of planets on the local protoplanetary disk, for instance as in a number of recent papers (Cleeves et al. 2015; Cridland et al. 2017; Stamatellos & Inutsuka 2018; Rab et al. 2019). Within the simplification of a spherical accretion geometry, our results show that essentially all of the accretion shock luminosity is expected to reach the local nebula, and that a high Rosseland optical depth, at least up to $\Delta\tau_R \sim 10$, does not lead to significant extinction of the bolometric shock luminosity in the accretion flow.

Finally, we have explored by different means whether our results point toward hot starts or cold starts (Section 7.1). As discussed above, the heating of the planet by the shock Q_{shock}^+ (i.e., the flow rate of inward-going energy; Equation (48)) was estimated to be much higher than the internal luminosity for the Marley et al. (2007) classical cold starts. This suggests that they are not entirely realistic. As for the "nominal cold start" or the "hot start" assumption during accretion, Mordasini et al. (2017) showed that both lead to warm or even hot starts. Taken together, all of this might explain why direct-imaging observations, with the sole exception of 51 Eri b (Macintosh et al. 2015; Nielsen et al. 2019), have not found evidence for planets even consistent with cold starts.

ORCID iDs

Gabriel-Dominique Marleau ● https://orcid.org/0000-0002-2919-7500
Christoph Mordasini ● https://orcid.org/0000-0002-1013-2811
Rolf Kuiper ● https://orcid.org/0000-0003-2309-8963

References

Alibert, Y., Mordasini, C., Benz, W., & Winisdoerffer, C. 2005, A&A, 434, 343
Aoyama, Y., Ikoma, M., & Tanigawa, T. 2018, ApJ, 866, 84
Baraffe, I., Elbakyan, V. G., Vorobyov, E. I., & Chabrier, G. 2017, A&A, 597, A19
Baraffe, I., Vorobyov, E., & Chabrier, G. 2012, ApJ, 756, 118
Baruteau, C., Bai, X., Mordasini, C., & Mollière, P. 2016, SSRv, 205, 77
Bell, K. R., & Lin, D. N. C. 1994, ApJ, 427, 987
Berardo, D., & Cumming, A. 2017, ApJL, 846, L17
Berardo, D., Cumming, A., & Marleau, G.-D. 2017, ApJ, 834, 149
Bodenheimer, P., D'Angelo, G., Lissauer, J. J., Fortney, J. J., & Saumon, D. 2013, ApJ, 770, 120
Bodenheimer, P., Hubickyj, O., & Lissauer, J. J. 2000, Icar, 143, 2
Bowler, B. P. 2016, PASP, 128, 38
Bowler, B. P., & Nielsen, E. L. 2018, Occurrence Rates from Direct Imaging Surveys (Berlin: Springer), 155k
Chauvin, G., Lagrange, A.-M., Dumas, C., et al. 2004, A&A, 425, L29
Cleeves, L. I., Bergin, E. A., & Harries, T. J. 2015, ApJ, 807, 2
Commerçon, B., Audit, E., Chabrier, G., & Chièze, J.-P. 2011a, A&A, 530, A13
Commerçon, B., Teyssier, R., Audit, E., Hennebelle, P., & Chabrier, G. 2011b, A&A, 529, A35
Cridland, A. J., Pudritz, R. E., Birnstiel, T., Cleeves, L. I., & Bergin, E. A. 2017, MNRAS, 469, 3910
Cumming, A., Helled, R., & Venturini, J. 2018, MNRAS, 477, 4817
Cuzzi, J. N., Estrada, P. R., & Davis, S. S. 2014, ApJS, 210, 21
D'Angelo, G., & Bodenheimer, P. 2013, ApJ, 778, 77
Drake, R. P. 2006, High-Energy-Density Physics: Fundamentals, Inertial Fusion, and Experimental Astrophysics (Berlin: Springer)
Drake, R. P. 2007, PhPl, 14, 043301
Ensman, L. 1994, ApJ, 424, 275
Geroux, C., Baraffe, I., Viallet, M., et al. 2016, A&A, 588, A85
González, M., Audit, E., & Huynh, P. 2007, A&A, 464, 429
Grassi, T., Bovino, S., Haugbølle, T., & Schleicher, D. R. G. 2017, MNRAS, 466, 1259
Hanawa, T., & Audit, E. 2014, JQSRT, 145, 9
Hartmann, L., Cassen, P., & Kenyon, S. J. 1997, ApJ, 475, 770
Hartmann, L., Herczeg, G., & Calvet, N. 2016, ARA&A, 54, 135
Helling, C., Winters, J. M., & Sedlmayr, E. 2000, A&A, 358, 651
Hosokawa, T., & Omukai, K. 2009, ApJ, 691, 823
Hosokawa, T., Yorke, H. W., Inayoshi, K., Omukai, K., & Yoshida, N. 2013, ApJ, 778, 178
Hubickyj, O., Bodenheimer, P., & Lissauer, J. J. 2005, Icar, 179, 415

Iglesias, C. A., Rogers, F. J., & Wilson, B. G. 1992, ApJ, 397, 717
Isella, A., & Natta, A. 2005, A&A, 438, 899
Jensen, S. S., & Haugbølle, T. 2018, MNRAS, 474, 1176
Jiang, Y.-F., Cantiello, M., Bildsten, L., Quataert, E., & Blaes, O. 2015, ApJ, 813, 74
Jiang, Y.-F., Stone, J. M., & Davis, S. W. 2014, ApJS, 213, 7
Kataoka, A., Okuzumi, S., Tanaka, H., & Nomura, H. 2014, A&A, 568, A42
Kirchschlager, F., Bertrang, G. H.-M., & Flock, M. 2019, MNRAS, 488, 1211
Klahr, H., & Kley, W. 2006, A&A, 445, 747
Klassen, M., Kuiper, R., Pudritz, R. E., et al. 2014, ApJ, 797, 4
Kley, W. 1989, A&A, 208, 98
Kuiper, R., Klahr, H., Dullemond, C., Kley, W., & Henning, T. 2010, A&A, 511, A81
Kuiper, R., & Yorke, H. W. 2013, ApJ, 772, 61
Levermore, C. D. 1984, JQSRT, 31, 149
Levermore, C. D., & Pomraning, G. C. 1981, ApJ, 248, 321
Lissauer, J. J., Hubickyj, O., D'Angelo, G., & Bodenheimer, P. 2009, Icar, 199, 338
Machida, M. N., Kokubo, E., Inutsuka, S.-i., & Matsumoto, T. 2008, ApJ, 685, 1220
Macintosh, B., Graham, J. R., Barman, T., et al. 2015, Sci, 350, 64
Malygin, M. G., Klahr, H., Semenov, D., Henning, T., & Dullemond, C. P. 2017, A&A, 605, A30
Malygin, M. G., Kuiper, R., Klahr, H., Dullemond, C. P., & Henning, T. 2014, A&A, 568, A91
Marleau, G.-D., Coleman, G. A. L., Leleu, A., & Mordasini, C. 2019, A&A, 624, A20
Marleau, G.-D., & Cumming, A. 2014, MNRAS, 437, 1378
Marleau, G.-D., Klahr, H., Kuiper, R., & Mordasini, C. 2017, ApJ, 836, 221
Marley, M. S., Fortney, J. J., Hubickyj, O., Bodenheimer, P., & Lissauer, J. J. 2007, ApJ, 655, 541
Marois, C., Macintosh, B., Barman, T., et al. 2008, Sci, 322, 1348
McClarren, R. G., & Drake, R. P. 2010, JQSRT, 111, 2095
Mignone, A., Bodo, G., Massaglia, S., et al. 2007, ApJS, 170, 228
Mignone, A., Zanni, C., Tzeferacos, P., et al. 2012, ApJS, 198, 7
Mihalas, D., & Mihalas, B. W. 1984, Foundations of Radiation Hydrodynamics (Oxford: Oxford Univ. Press)
Mordasini, C. 2013, A&A, 558, A113
Mordasini, C., Alibert, Y., Georgy, C., et al. 2012a, A&A, 547, A112
Mordasini, C., Alibert, Y., Klahr, H., & Henning, T. 2012b, A&A, 547, A111
Mordasini, C., Marleau, G.-D., & Mollière, P. 2017, A&A, 608, A72
Nielsen, E. L., De Rosa, R. J., Macintosh, B., et al. 2019, arXiv:1904.05358
Paxton, B., Bildsten, L., Dotter, A., et al. 2011, ApJS, 192, 3
Paxton, B., Cantiello, M., Arras, P., et al. 2013, ApJS, 208, 4
Paxton, B., Marchant, P., Schwab, J., et al. 2015, ApJS, 220, 15
Paxton, B., Schwab, J., Bauer, E. B., et al. 2018, ApJS, 234, 34
Pollack, J. B., Hollenbach, D., Beckwith, S., et al. 1994, ApJ, 421, 615
Pollack, J. B., Hubickyj, O., Bodenheimer, P., et al. 1996, Icar, 124, 62
Rab, C., Kamp, I., Ginski, C., et al. 2019, A&A, 624, A16
Rafikov, R. R. 2016, ApJ, 831, 122
Santamaría-Miranda, A., Cáceres, C., Schreiber, M. R., et al. 2018, MNRAS, 475, 2994
Saumon, D., Chabrier, G., & van Horn, H. M. 1995, ApJS, 99, 713
Semenov, D., Henning, T., Helling, C., Ilgner, M., & Sedlmayr, E. 2003, A&A, 410, 611
Stahler, S. W. 1988, ApJ, 332, 804
Stahler, S. W., Shu, F. H., & Taam, R. E. 1980, ApJ, 241, 637
Stamatellos, D., & Inutsuka, S.-i 2018, MNRAS, 477, 3110
Szulágyi, J., Masset, F., Lega, E., et al. 2016, MNRAS, 460, 2853
Szulágyi, J., Mayer, L., & Quinn, T. 2017, MNRAS, 464, 3158
Szulágyi, J., & Mordasini, C. 2017, MNRAS, 465, L64
Tanigawa, T., Ohtsuki, K., & Machida, M. N. 2012, ApJ, 747, 47
Tazaki, R., Tanaka, H., Kataoka, A., Okuzumi, S., & Muto, T. 2019, arXiv:1907.00189
Turner, N. J., & Stone, J. M. 2001, ApJS, 135, 95
Uyama, T., Tanigawa, T., Hashimoto, J., et al. 2017, AJ, 154, 90
Vaytet, N., Chabrier, G., Audit, E., et al. 2013a, A&A, 557, A90
Vaytet, N., González, M., Audit, E., & Chabrier, G. 2013b, JQSRT, 125, 105
Wagner, K., Apai, D., & Kratter, K. M. 2019, arXiv:1904.06438
Zel'dovich, Y. B., & Raizer, Y. P. 1967, Physics of Shock Waves and High-temperature Hydrodynamic Phenomena (New York: Academic)